Molecular Nanocomposites with Lanthanide- and Counter-Cation-Mediated Interfacial Electron Transfer between Phthalocyanine and Polyoxovanadate

Irina Werner,[a] Jan Griebel,[a] Albert Masip-Sánchez,[b] Xavier López,*[b] Karol Załęski,[c] Piotr Kozłowski,*[d] Axel Kahnt,[a] Martin Boerner,[a,e] Ziyan Warneke,[a,f] Jonas Warneke,[a,f] and Kirill Yu. Monakhov*[a]

[a] *Leibniz Institute of Surface Engineering (IOM), Permoserstr. 15, 04318 Leipzig, Germany*

[b] *Universitat Rovira i Virgili, Departament de Química Física i Inorgànica, Marcel·lí Domingo 1, 43007 Tarragona, Spain*

[c] *NanoBioMedical Centre, Adam Mickiewicz University in Poznań ul. Wszechnicy Piastowskiej 3, 61-614 Poznań, Poland*

[d] *Institute of Spintronics and Quantum Information, Faculty of Physics, Adam Mickiewicz University in Poznań, ul. Uniwersytetu Poznańskiego 2, 61-614 Poznań, Poland*

[e] *Institute of Inorganic Chemistry, Leipzig University, Johannisallee 29, 04103 Leipzig, Germany.*

[f] *Wilhelm-Ostwald-Institute for Physical and Theoretical Chemistry, Leipzig University, Linnéstr. 2, 04103 Leipzig, Germany.*

ABSTRACT: A series of $\{V_{12}\}$-nuclearity polyoxovanadate cages covalently functionalized with one or sandwiched by two phthalocyaninato (Pc) lanthanide (Ln) moieties via V−O−Ln bonds were prepared and fully characterized for paramagnetic Ln = Sm^{III}–Er^{III} and diamagnetic Ln = Lu^{III}, including Y^{III}. The LnPc-functionalized $\{V_{12}O_{32}\}$ cages with fully-oxidized vanadium centers in the ground state were isolated as $(n\text{Bu}_4\text{N})_3[HV_{12}O_{32}Cl(LnPc)]$ and $(n\text{Bu}_4\text{N})_2[HV_{12}O_{32}Cl(LnPc)_2]$ compounds. As corroborated by a combined experimental (EPR, DC and AC SQUID, laser photolysis transient absorption spectroscopy, electrochemistry) and computational methods (DFT, MD, model Hamiltonian approach), the compounds feature *intra*- and *inter*molecular electron transfer that is responsible for a partial reduction at V(3d) centers from V^V to V^{IV} in the solid state and at high sample concentrations. The effects are generally Ln-dependent and are clearly demonstrated for the $(n\text{Bu}_4\text{N})_3[HV_{12}O_{32}Cl(LnPc)]$ representative with Ln = Lu^{III} or Dy^{III}. *Intra*molecular charge transfer takes place for Ln = Lu^{III} and occurs from a Pc ligand *via* the Ln center to the $\{V_{12}O_{32}\}$ core of the same molecule, whereas for Ln = Dy^{III} only *inter*molecular charge transfer is allowed, which is realized from Pc in one molecule to $\{V_{12}O_{32}\}$ core of another molecule usually via the $n\text{Bu}_4N^+$ counter-cation. For all Ln but Dy^{III} two of these phenomena may be present in different proportions. Besides, it is demonstrated that $(n\text{Bu}_4\text{N})_3[HV_{12}O_{32}Cl(DyPc)]$ is a field induced single molecule magnet with a maximal relaxation time of order 10^{-3} s. The obtained results open up the way to further exploration and fine-tuning of these three-modular molecular nanocomposites regarding tailoring and control of their Ln-dependent charge-separated states (induced by *intra*-molecular transfer) and relaxation dynamics as well as of electron hopping between molecules. This should enable to realize ultra-sensitive polyoxometalate powered quasi-superconductors, sensors, and data storage/processing materials for quantum technologies.

INTRODUCTION

Polyoxometalates (POMs),[1] molecular metal–oxides, show well-defined nanoscale spatial structures[2] carrying a negative charge that is balanced by surrounding counterions.[3] In solution, these inorganic complexes tend to spontaneously form low-to-high dimensional self-assemblies, exploiting forces between different weakly interacting particles (POM, cation, solvent molecule).[4] Introducing an organic functionality onto POM[5–7] provides an additional and most effective lever for controlling and programming these interactions at the charge- and spin-state[8,9] level. Such an interplay between POM's coordination and supramolecular[10] chemistry and POM's electronic structure[11] opens up a wide range of possibilities for developing early models of functional hybrid quantum systems, with POMs as spin qubits or POMs as quantum sensors. The POM-based devices would thus enable to store, process, or sense the information through cooperative *intra*- and *inter*molecular effects.

The covalent combination of POMs with transition metal (TM) or lanthanide[12,13] (Ln) ions embedded into redox-active phthalocyanine (Pc^{2-}) macrocycles has emerged as a good compromise to address this challenge. Unlike the well-described electrostatic interactions of phthalocyanines and POMs,[14–19] there are only a few reports addressing effects of their covalent interaction.[20,21] Drain and co-workers synthesized hybrid compounds[20] $(n\text{Bu}_4\text{N})_5[PW_{11}O_{39}(TMPc)]$ (TM = Zr^{4+} or Hf^{4+}) where a transition metal–Pc moiety is directly grafted onto the fully-oxidized, lacunary Keggin-type POM. It was demonstrated that the metal ions mediate the electronic communication between the Pc and the Keggin-POM units. Later, the LnPc-functionalized analogues, $[PW_{11}O_{39}(LnPc)]^{6-}$ (Ln = Tb^{III}, Dy^{III} and Y^{III}) were introduced by Kögerler and co-workers, whereby for the Dy^{III}-containing species slow relaxation of the magnetization was observed.[21] In two other related studies, we delivered appealing pre-conditions for building up stimuli-responsive POM quantum networks based on LnPc-functionalized POMs with

fully-oxidized V(3d) centres[22] and/or reduced vanadyl (VO^{2+}) groups[23,24] (hereafter referred to as V-POMs[25]). Firstly, we showed[26] that compounds consisting of the electron-donor phthalocyaninato lanthanide moiety and the electron-acceptor V_3-substituted Wells-Dawson-type POM structure, linked covalently to each other *via* a pyridine-augmented tris(alkoxo) ligand, exhibit *intra-* and *inter*molecular ground-state charge transfer. It might thus be used to tailor electron communication within quantum networks. Secondly, enabling direct interaction between V-POM and LnPc we succeeded[27] in the synthesis of structurally robust, electron correlated compounds $[V_{12}O_{32}Cl(YbPc)_n]^{n-5}$ (n = 1 or 2), in which the dodecavanadate cage is covalently capped by one or sandwiched by two YbPc moieties.

Building upon this work,[27] we now report on a broad spectrum of unique chemical physics of $[HV_{12}O_{32}Cl(LnPc)_n]^{n-4}$ compounds for Ln = Sm^{III}–Er^{III}, Lu^{III} and Y^{III} (hereafter referred to as PcLn-{V_{12}} for n = 1 and $(PcLn)_2$-{V_{12}} for n = 2) using a combination of experimental and computational techniques. It is noteworthy that the fully-oxidized, lacunary-type {$V_{12}O_{32}$}-cage[28] has been shown in numerous studies to be an excellent scaffold for functionalization with 3d-,[29–31] 4f-[32–34] and alkaline-earth metal ions.[35–37] Cronin and co-workers were first to present a series of $(nBu_4N)_2[LnV_{12}O_{32}Cl](H_2O)_2(CH_3CN)_2$ compounds with late Ln ions (Gd^{III}–Er^{III}) directly incorporated into the dodecavanadate cage.[33] Magnetic measurements revealed, however, the free Ln ion behavior. Practically simultaneously, Powell and co-workers described an unusual cationic version of the {V_{12}}-nuclearity cage functionalized with two Ln ions (Ln = Gd^{III}–Er^{III}).[34]

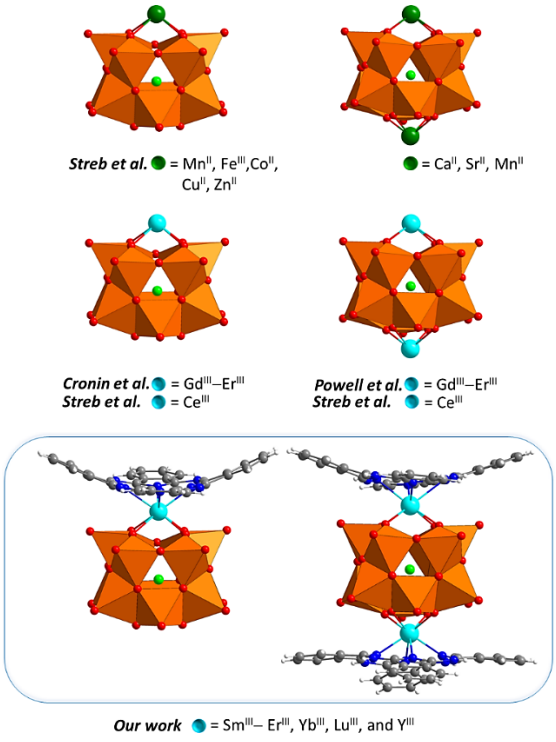

Figure 1. An overview of literature-known mono- and bis-heterometal-functionalized {$V_{12}O_{32}$} cages (top and middle) and new $(PcLn)_n$-{V_{12}} hybrids with n = 1 or 2 (bottom). Colour code: VO_5 polyhedra = orange, O = red, Cl = green, C = dark grey, N = blue, H = white. Solvent ligands (top and middle), counterions (in all examples), and H atoms at the {$V_{12}O_{32}$} cage (bottom) are not shown.

An elegant method for the synthesis of metal functionalized $[V^{V}_{12}O_{32}Cl]^{5-}$ using a "placeholder" strategy was introduced by Streb and co-workers.[29–32,36,37] For instance, stepwise functionalization of $(nBu_4N)_3(Me_2NH_2)_2[V_{12}O_{32}Cl]$, where the dimethylammonium cation assumes the placeholder function, with transition metal ions[29–31] or with an early Ln[32] representative Ce^{III} resulted in mono- and bis-substituted vanadium–oxo clusters with enhanced redox activity. This ability of the $[V^{V}_{12}O_{32}Cl]^{5-}$ polyoxoanion to act as an electron reservoir, without undergoing substantial structural transformation,[38] was also used to stabilize low-valent Fe^{I} species.[31]

In this Article, we showcase the underlying formation and mechanism of action of highly promising donor–acceptor nanocomposites consisting of one or two LnPc moieties ligated to the {$V_{12}O_{32}$} cage (Figure 1). The produced mono-substituted $(nBu_4N)_3[HV_{12}O_{32}(Cl)](LnPc)$ (hereafter referred to as PcLn-{V_{12}}) and bis-substituted $(nBu_4N)_2[HV_{12}O_{32}(Cl)](LnPc)_2$ (hereafter referred to as $(PcLn)_2$-{V_{12}}) compounds feature the *intra*molecular charge transfer and redox-promoted magnetism. The electron communication between the individual compounds containing paramagnetic Sm^{III}–Er^{III} or diamagnetic Lu^{III} and Y^{III} ions is realized within their supramolecular self-assembly that is generated due to *inter*molecular interactions involving V-POM, LnPc, and counterion units. The future controlled immobilization, electronical modification, and electrical contacting of these nanocomposites on surfaces might lead to the creation of scalable 'molecularly powered quantum network-on-a-chip' electronics for neurocomputing and ultra-sensitive electrical and magnetic signal detection.

RESULTS AND DISCUSSION

Synthesis and structure characterization

Monophthalocyanine lanthanide acetate complexes (PcLnOAc) with Ln = Sm^{III}–Er^{III}, Lu^{III} and Y^{III} were synthesized similarly to the protocols described in the literature.[39,27] Repeated purification by column chromatography and subsequent slow evaporation of PcLnOAc·MeOH·H_2O in wet ethanol delivered high-quality PcLnOAc·EtOH·H_2O crystals for Ln = Sm^{III}, Dy^{III}, Lu^{III} and Y^{III} (see the Supporting Information). The synthesis of PcLnOAc with earlier lanthanides (Ln = La^{III}–Nd^{III}) was not successful likely due to their larger ionic radii.

The subsequent reaction of one or two equivalents of PcLnOAc·MeOH·H_2O with $(nBu_4N)_4[HV_{12}O_{32}Cl]$[28] was carried out according to the synthetic routes developed in our previous Communication[27] for $[V_{12}O_{32}Cl(YbPc)_n]^{n-5}$ with n = 1 or 2 (see the Supporting Information). CHN elemental analysis, thermogravimetric (TG) measurements, IR- and UV-Vis-spectroscopy and ^{1}H NMR spectra (for PcLu-{V_{12}}) of powder samples confirmed the identity and the purity of the synthesized compounds as well as the presence of three and two nBu_4N^+ counter-cations *per* {V_{12}} in PcLn-{V_{12}} and $(PcLn)_2$-{V_{12}} compounds, respectively (see the Supporting Information).

Needle-shaped green crystals, suitable for X-ray analysis were obtained for $(nBu_4N)_3[HV_{12}O_{32}Cl(YPc)](CH_3CN)_4$ by slow diffusion of di-*iso*-propylether into an acetonitrile solution. In the case of bis-substituted compounds plate-shaped blue crystals with the formula $(nBu_4N)_3[V_{12}O_{32}Cl(LnPc)_2](CH_3CN)_3$ (Ln = Dy^{III}, Ho^{III}) were isolated by slow evaporation of an acetonitrile/dichloromethane solution (see the Supporting Information).

High resolution negative-mode ESI-MS of PcLn-{V_{12}} and $(PcLn)_2$-{V_{12}} also confirmed in both cases the presence of the corresponding compounds (see the Supporting Information). For example, in the ESI mass spectrum of PcLu-{V_{12}} alongside with the $[HV^{V}_{12}O_{32}(Cl)](LuPc)]^{3-}$ ion, containing a fully-oxidized {$V_{12}O_{32}$} cage, a mixture of $[(nBu_4N)_2[HV^{IV}V^{V}_{11}O_{32}Cl](LuPc)]^{2-}$ and $[(nBu_4N)_2[V^{V}_{12}O_{32}Cl](LuPc)]^{2-}$ in a ratio of 1:1 combining both the fully-oxidized and the one-electron-reduced vanadium–oxo clusters, respectively, was detected. Signals indicating the presence of the one-electron-reduced {$V^{IV}V^{V}_{11}$}, core in PcLn-{V_{12}} could also be observed in Eu^{III}-, Gd^{III}-, Tb^{III}- and Dy^{III}-analogues. In nearly all bis-substituted $(PcLn)_2$-{V_{12}} derivatives the prevailing number of signals was attributed to the ions with a {$V^{IV}V^{V}_{11}$} electron population.

For both PcLu-{V_{12}} and $(PcLu)_2$-{V_{12}} molecular nanocomposites, X-ray photoelectron spectroscopy (XPS) of their powder samples confirms the presence of $V^{IV}O^{2+}$ units in the {V_{12}} core. It is evidenced by the presence of a broad structured line with a shoulder in the $V2p_{3/2}$ region (Figures S53 and S54). $O1s/V2p_{3/2}$ binding energy differences of 12.9 eV and 14.2 eV were assigned to V^{V} and V^{IV}, respectively. These findings agree with the values reported previously for Ca_2-{V_{12}} containing a partially reduced dodecavanadate cage.[36]

Electrochemical analysis

The redox properties of the selected PcLn-{V_{12}} compounds were studied by recording the cyclic voltammograms in CH_2Cl_2 solution using tetra-*n*-butylammonium hexafluorophosphate (NBu_4PF_6) as an electrolyte at a scan rate of 100 $mV{\cdot}s^{-1}$. The redox potentials are reported against Fc^+/Fc. The comparison of the cyclic voltammograms of PcLu-{V_{12}}, PcGd-{V_{12}} and PcDy-{V_{12}} in the –1 V to +1 V potential range shows that the electrochemical properties of the compounds are very similar and feature four quasi-reversible redox processes, namely one reductive transition (R_1) and three oxidative processes (O_1, O_2 and O_3).

Table 1. Overview of the electrochemically studied compounds and their half-wave potentials for each determined redox process.

	R_1 / [V] ($V^{V}\rightarrow V^{IV}$)	O_1 / [V] ($V^{IV}\rightarrow V^{V}$)	O_2 / [V] ($Pc\rightarrow Pc^{\bullet+}$)	O_3 / [V] ($Pc^{\bullet+}\rightarrow Pc^{2+}$)
{V_{12}}	–0.37	–	–	–
PcLu-{V_{12}}	–0.50	–0.07	0.30	0.72
PcGd-{V_{12}}	–0.45	0.00	0.36	0.73
PcDy-{V_{12}}	–0.37	0.00	0.32	0.73

The nature of the lanthanide ion, though, influences slightly the redox activity of the compounds resulting in overall cathodic shifts in Gd^{III}- and Dy^{III}-containing representatives (Figure 2). Mean peak potentials for the investigated nanocomposites are listed in Table 1. The nature of compounds' redox waves was determined by comparison with the corresponding precursors, i.e. $(nBu_4N)_4[HV_{12}O_{32}Cl]$ and PcLnOAc (Figure S55). The most interesting feature in all cyclic voltammograms is the appearance of the new redox process O_1, which can be assigned to the oxidation of V^{IV} in the {$V_{12}O_{32}$} cage matching earlier reports for one electron-reduced dodecavanadate bis-functionalized with Ce^{III}.[37] $(PcLn)_2$-{V_{12}} compounds show comparable results with those obtained for PcLn-{V_{12}}. For example, the $(PcLu)_2$-{V_{12}} is characterized by small cathodic shifts and low peak-current for all redox processes compared to the mono-substituted derivative (Figure S55).

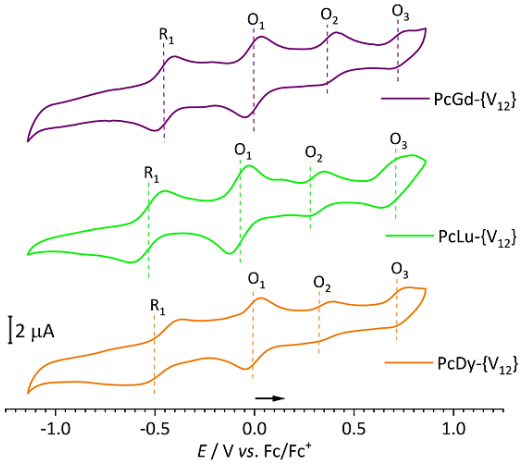

Figure 2. Cyclic voltammograms of PcLu-{V_{12}} (c = 0.4 x 10^{-3}), PcGd-{V_{12}} (c = 0.4 x 10^{-3}) and PcDy-{V_{12}} (c = 0.4 x 10^{-3}) in CH_2Cl_2 solution of NBu_4PF_6 (c = 1 x 10^{-1}) at the scan rate of 100 $mV{\cdot}s^{-1}$ *vs.* Fc^+/Fc.

Solid-state and solution EPR studies

EPR is a highly sensitive and a powerful tool for detecting unpaired spins in paramagnetic substances and, thus, of utmost importance for monitoring redox events in compounds such as polyoxovanadates,[24] where vanadium ions may simultaneously act as charge and spin carriers. For instance, the striking role of EPR has been demonstrated for non-photoinduced charge transfer between MPc (M = Yb^{III} or Y^{III}) moieties and a {V_3}-substituted Wells-Dawson-type POM, which are linked to each other by an insulating organic spacer.[26] Polycrystalline PcLuOAc showed similar EPR characteristics (Figure S57), as reported earlier for PcYOAc,[26] featured by an isotropic signal with a g value of 2.002 and a line width ΔB_{PP} = 0.38 mT. The shape of the EPR signal and the g value point out a ligand-centered (specifically, carbon-centered) freely delocalized electron, excluding other paramagnetic impurities.

Monophthalocyaninato acetate complexes of other paramagnetic lanthanides explored in this study are EPR silent due to very fast spin-lattice relaxation time at room temperature, typical for lanthanide ions. This is in accordance with earlier EPR studies of neutral bis-phthalocyanine lanthanide complexes with a permanent radical character.[40] In the case of PcGdOAc, which is distinguished by its relatively long spin-lattice relaxation time, a broad EPR signal induced by a large spin-spin interaction between Gd^{III} ions was observed (Figure S57). Concentration-dependent measurements of PcLuOAc in CH_2Cl_2 (Figure S58) showed that the radical character is barely detectible at very low concentrations. These findings are in accordance with those reported for metal-free phthalocyanines,[41] closed-shell molecules exhibiting condensed-phase paramagnetism, which is typical for planar π-extended systems with high-lying HOMOs.[42]

The solid-state EPR spectra of the equal amounts of polycrystalline powdered samples of PcLu-{V_{12}} and (PcLu)$_2$-{V_{12}} (Figure 3) display in both cases, beside a radical character (with a *g* value = 2.002 each), a central line with large shoulders with

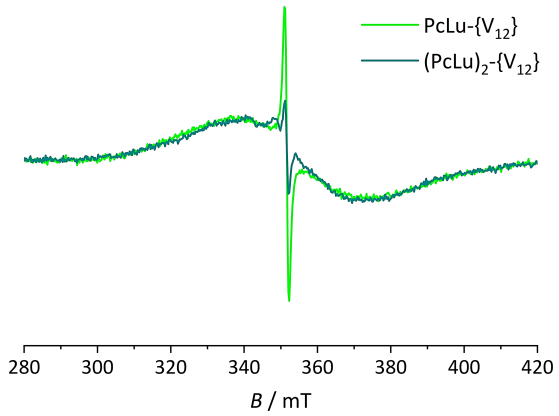

Figure 3. Solid-state X-band EPR spectra of PcLu-{V_{12}} (green) and (PcLu)$_2$-{V_{12}} (dark cyan) measured at r.t. at a frequency of 9.44 GHz, modulation amplitude of 0.1 mT, and microwave power of 0.2 mW. Normalised double integration values: PcLu-{V_{12}} = $2.97{\cdot}10^8$ (10 mg, 3.7 mmol), (PcLu)$_2$-{V_{12}} = $3.07{\cdot}10^8$ (11.5 mg, 3.7 mmol)

the *g* values of 1.997 and 1.985, respectively. The shape of the signals as well as the calculated *g* values are typical for V^{IV} ions constitutive of polyoxovanadates in which electrons are delocalized over more than one V^{IV} center.[43–46] Although the presence of a radical is more pronounced in PcLu-{V_{12}} as compared to (PcLu)$_2$-{V_{12}}, the intensities of the V^{IV} signals are practically similar in both cases.

The analysis of the unit cell packings of PcY-{V_{12}} and (PcDy)$_2$-{V_{12}} (Figures S62 and S63) showed that both systems feature a layer structure, where the corresponding hybrid anions are separated by the nBu$_4$N$^+$ counter-cations, thus lacking any direct π-π-stacking interactions or hydrogen bonding between the units as in the case of PcLnOAc. These findings lead to the conclusion that the *inter*molecular charge transfer in the solid state is likely transmitted by nBu$_4$N$^+$ in the systems PcLn-{V_{12}} or (PcLn)$_2$-{V_{12}}. Lately, it has been recognized that the interactions between POMs and counter-cations are not limited to mere charge balance but are also crucial for the structure-induced-reactivity of POMs, charge transport characteristics in molecular junctions and electrical conductivity.[3,47,48]

Solid-state EPR spectra of the equal amounts (each 3.7 mmol) of other polycrystalline powdered samples of paramagnetic PcLn-{V_{12}} and (PcLn)$_2$-{V_{12}} hybrid compounds (Ln = Sm^{III}–Eu^{III}, Tb^{III}–Yb^{III}) revealed only broad V^{IV}-based signals (see Figure 4 for PcLn-{V_{12}} compounds with the corresponding listed *g* values and normalized double integration values). The EPR spectra of PcGd-{V_{12}} and (PcGd)$_2$-{V_{12}} showed a broad overlap of signals probably originating from V^{IV} and f electrons of Gd^{III}, so that the *g* values could not be determined (Figure S59).

The comparison of the V^{IV} signal integration of the paramagnetic PcLn-{V_{12}} representatives among each other qualitatively shows that in the case of the prolate ions[49] Sm^{III}, Er^{III} and Yb^{III} the spin density is higher than that where highly oblate Dy^{III} and Tb^{III} (except for Ho^{III}) are involved. Further investigations applying high-field EPR at low temperature are the focus of our future research on the quantification of the coupling between the magnetic moments of Ln^{III} ions and the free delocalized electron[50] as well as its impact on the *intra*molecular charge transfer from the LnPc moiety to the {V_{12}} unit.

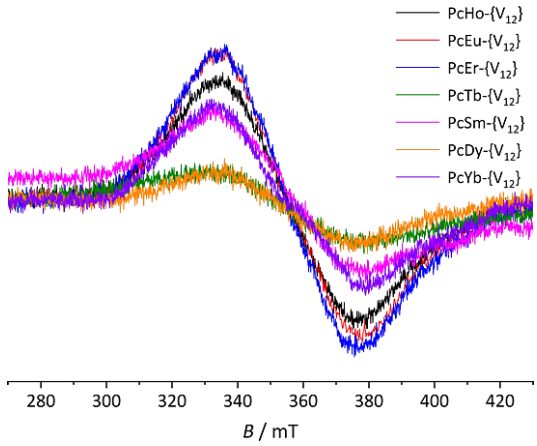

Figure 4. Solid-state X-band EPR spectra of paramagnetic PcLn-{V_{12}} (Ln = Sm^{III}–Eu^{III}, Tb^{III}–Yb^{III}) with detected V^{IV} signals. Spectra were measured at r.t. at a frequency of 9.44 GHz, modulation amplitude of 0.1 mT, and microwave power of 0.2 mW with the following *g* values: 1.977 (Sm^{III}), 1.984 (Eu^{III}), 1.993 (Tb^{III}), 1.985 (Dy^{III}), 1.984 (Er^{III}), 1.987 (Ho^{III}) and 1.986 (Yb^{III}). Color code: Sm^{III} = magenta, Eu^{III} = red, Tb^{III} = dark green, Dy^{III} = orange, Er^{III} = blue, Ho^{III} = black, Yb^{III} = violet. Normalized double integration values: PcHo-{V_{12}} = $3.12{\cdot}10^5$, PcEu-{V_{12}} = $3.57{\cdot}10^5$, PcEr-{V_{12}} = $3.81{\cdot}10^5$, PcTb-{V_{12}} = $2.56{\cdot}10^4$, PcSm-{V_{12}} = $9.05{\cdot}10^4$, PcDy-{V_{12}} = $1.94{\cdot}10^4$, PcYb-{V_{12}} = $2.48{\cdot}10^5$.

As a proof-of-concept, that the reduction of the {V_{12}}-nuclearity cage is due to the charge transfer from the Pc moiety, we also investigated (nBu$_4$N)$_2$[LnV$_{12}$O$_{32}$(Cl)](H$_2$O)$_2$(CH$_3$CN)$_2$ (Ln = Gd^{III}, Dy^{III}, Ho^{III}, Yb^{III} and Y^{III}) that were synthesized according to the published procedure[33] (see the Supporting Information) .

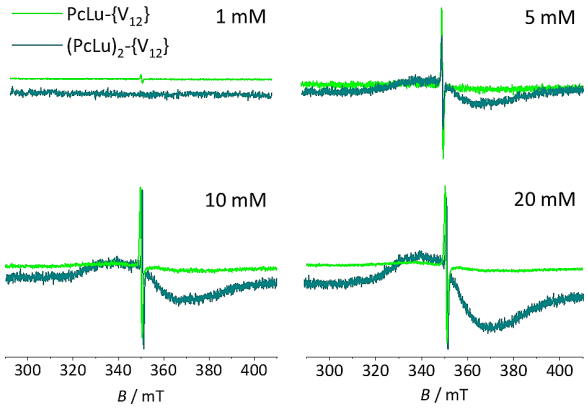

Figure 5. Solution EPR spectra of PcLu-{V_{12}} (green) and (PcLu)$_2$-{V_{12}} (dark cyan) at concentrations 1–20 mM measured at r.t. at a frequency of 9.44 GHz, modulation amplitude of 0.1 mT, and microwave power of 0.2 mW.

The compounds proved to be EPR silent, except for Gd^{III}-caped {$V_{12}O_{32}$} cage characterized only by the signal with the

g value of 1.987 (Figure S60) that is typical for Gd^{III} hydrated salts.[51]

Concentration dependent EPR measurements of PcLu-{V_{12}} and $(PcLu)_2$-{V_{12}} between 1 mM and 20 mM in CH_2Cl_2 showed that in PcLu-{V_{12}} a weak radical character is already present at 1 mM, whereas $(PcLu)_2$-{V_{12}} is EPR silent at the same concentration. Further increase in concentration was accompanied by a continuous increase of the radical character (up to 10 mM) in both compounds, but only in $(PcLu)_2$-{V_{12}} the growth of the V^{IV} signals was observed throughout the concentration series (Figure 5).

These findings differ from those observed for these compounds in the solid state, where the intensities of V^{IV} signals for both mono- and bis-functionalized derivatives are practically the same. To reveal obviously different underlying mechanisms of *inter*molecular charge transfer in the solid state and in solution, on the one hand, and between PcLn-{V_{12}} and $(PcLn)_2$-{V_{12}} in solution, on the other hand, we next conducted computational study on these molecular nanocomposites (*vide infra*).

Computational studies

Classical molecular dynamics (MD) and density functional theory (DFT) calculations were carried out for PcLn-{V_{12}} and $(PcLn)_2$-{V_{12}} compounds to investigate: *i*) their dynamic behavior in solution at low and high concentrations, *ii*) their electronic structure and the distribution of unpaired electrons in fully-oxidized and one-electron reduced forms, and *iii*) the *intra*- and *inter*molecular electron transfer in the solid state. Understanding the electron mobility both in *intra*- and *inter*molecular fashions is highly relevant for the development of (conducting)[52] molecular quantum materials[53] based on donor–acceptor molecular systems. The following calculations represent the lower bounds of the real system since they do not include molecular vibrations, which can favor electron hopping processes due to the thermal energy.

MD simulations

Atomistic MD simulations with explicit solvent molecules were performed to determine the behavior of PcLn-{V_{12}} and $(PcLn)_2$-{V_{12}} (for Ln = Lu) in pure CH_2Cl_2 using the GROMACS 5.1.2 code[54,55] and a modified AMBER 99 Force Field,[56] which has been successfully employed in previous studies of the dynamic behavior of POMs in different environments, including aggregation phenomena.[57–59] The MD trajectories were calculated imposing 3D periodic boundary conditions. Two different fundamental cubic boxes were used: a $(8.5\ nm)^3$ box containing 8 units (PcLn-{V_{12}} or $(PcLn)_2$-{V_{12}} anions) for the 20 mM (high concentration) solution, and a $(11.6\ nm)^3$ box containing 5 units for the 5 mM (low concentration) solution. Each box contains an appropriate number of $n(Bu_4N^+)$ counter-cations to ensure the electroneutrality. All simulations were carried out at controlled $T = 300$ K by coupling the system to a thermal bath using the velocity-rescaling algorithm. Prior to the production runs, all systems were equilibrated by an initial 500 ps run at constant *NVT* fixing the solute, followed by a 500 ps run at constant *NPT* to readjust the box size, and a final 500 ps run at constant *NVT* with relaxed solute. Production trajectories simulate 40 ns with a canonical (*NVT*) ensemble, collecting data every 1 ps. The data from four different MD calculations, 5 mM and 20 mM solutions of PcLn-{V_{12}} and $(PcLn)_2$-{V_{12}}, were analyzed with the focus on the mode and the extent of the aggregation between the molecules. The most probable interaction modes are represented in Figure 6.

Aggregation of mono PcLn-{V_{12}} anions in solution is not strongly favored, but calculations suggest that it takes place mediated by $n(Bu_4N^+)$ counter-cations, which are located between directly confronted {V_{12}} units (see Figure 6, top). The anionic nature of the {V_{12}} region, and it being sterically highly exposed, keeps the $n(Bu_4N^+)$ units strongly attached to it *via* Coulomb attraction. Thus, we did not observe long-lived direct intermolecular Pc···{V_{12}} contacts (see Figure 7C, left panels), likely due to their poor mutual electrostatic and dispersive affinity, which cannot compete with the stronger $n(Bu_4N^+)$···{V_{12}} affinity in the mono complex. For the bis complex in solution, in contrast, intermolecular contacts between $(PcLn)_2$-{V_{12}} units can be long-lived (Figure 7C, right panels) and mostly occurs *via* π–π dispersive interactions between the Pc groups remarkably with no counter-cation-aided aggregation at all (as shown in Figures 6 (bottom) and 7D (bottom)). In addition, it can be inferred that the two bulky Pc groups in $(PcLn)_2$-{V_{12}} units largely reduce the probability of aggregation via {V_{12}}···{V_{12}} contacts —even if these were mediated by $n(Bu_4N^+)$ units— because counter-cations are less prone to attach to the more sterically protected {V_{12}} region in the bis complex. ~~Aggregation of PcLn-{V_{12}} anions (Figure 6, top) is mediated by $n(Bu_4N^+)$ units placed between the two vertically confronted {V_{12}} regions. The anionic nature of the {V_{12}} region keeps $n(Bu_4N^+)$ units strongly attached to it *via* Coulomb attraction. Moreover, due to the presence of only one Pc group in PcLn-{V_{12}} anion, the {V_{12}} region is highly exposed to $n(Bu_4N^+)$ counter-cations in solution. No long-lived Pc···{V_{12}} contacts were observed (see Figure 7C, left panels), likely due to their poor mutual electrostatic and dispersive affinity. In contrast, the aggregation of $(PcLn)_2$-{V_{12}} anions can be long-lived (Figure 7C, right panels) and mostly occurs *via* π–π dispersive interactions between the Pc groups as shown in Figure 7D (bottom) remarkably with no counter-cation aided aggregation at all. We suggest that the two bulky Pc groups in $(PcLn)_2$-{V_{12}} units reduce the probability of aggregation *via* the transversally oriented {V_{12}}···{V_{12}} pair, mainly because the $n(Bu_4N^+)$ units are not as prone to attach to {V_{12}} as they are in PcLn-{V_{12}}.~~

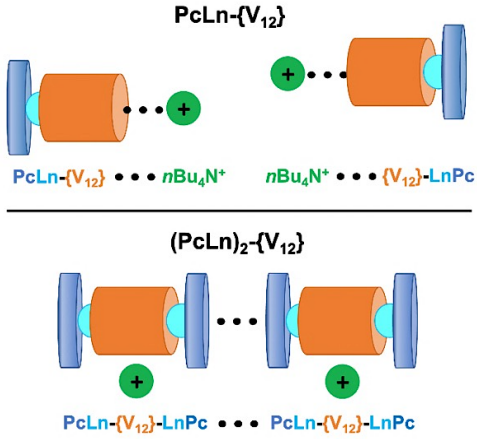

Figure 6. A schematic representation of preferable modes of *inter*molecular aggregation of dimers in solution in dependence on the number of LnPc ligands present in the respective compound. *Top*: Dimers of PcLn-{V_{12}} anions formed by the vertical interaction of two {V_{12}} regions with two $n(Bu_4N^+)$ counter-cations between them.

Bottom: Dimers of $(PcLn)_2$-$\{V_{12}\}$ anions resulting from the Pc···Pc interactions without nBu_4N^+-mediated aggregation. Not all nBu_4N^+ counter-cations are depicted for the sake of clarity.

As mentioned earlier, cation-assisted aggregation of POMs in solution is a well-known phenomenon.[57–59] With the increasing negative charge of the POM, Coulomb interactions become a decisive factor. In the present study, the PcLn-$\{V_{12}\}$ anion···nBu_4N^+ interaction, mainly *via* a nBu_4N^+···$\{V_{12}\}$ contact, is –912 kJ mol^{-1} *per* unit. This value is much higher than those calculated for the π–π interactions through the Pc···Pc contact (–152 kJ mol^{-1}) and for the less probable $(PcLn)_2$-$\{V_{12}\}$ anion···nBu_4N^+ interaction (–135 kJ mol^{-1}) in the $(PcLn)_2$-$\{V_{12}\}$ compound. In fact, the motions of nBu_4N^+ and $(PcLn)_2$-$\{V_{12}\}$ ions in CH_2Cl_2 solutions are practically uncorrelated.

Next, analysis based on the radial distribution function (RDF or $g(r)$) was performed to determine the concentration-dependent degree of dimer formation, taking into consideration that higher-order aggregates are much less common and ephemeral

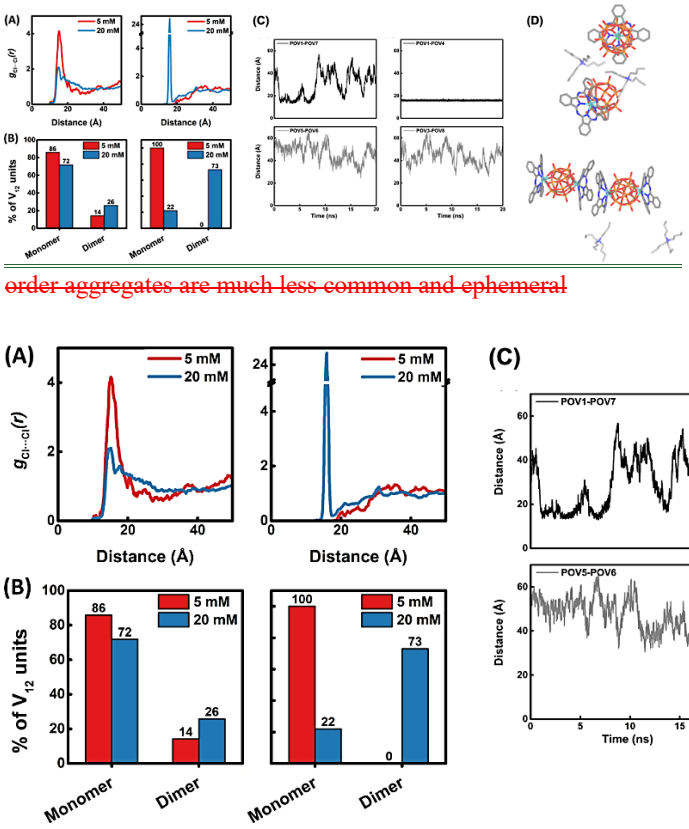

Figure 7. Molecular dynamics simulations of the behavior in solution. (A) Radial distribution functions (RDFs) between Cl centers of $\{V_{12}\}$ units for PcLn-$\{V_{12}\}$ (left) and $(PcLn)_2$-$\{V_{12}\}$ (right), Ln = Lu. Data ~~had been~~ taken every 2 ps from the last 20 ns of the~~MD~~ simulations. (B) State of aggregation, in %, of $\{V_{12}\}$ units of PcLn-$\{V_{12}\}$ (left) and $(PcLn)_2$-$\{V_{12}\}$ (right) compounds. Higher aggregated oligomers (trimers and higher, not displayed) represent less than 1%. (C) Distance vs time evolution of some POV···POV (polyoxovanadate···polyoxovanadate) pairs of PcLn-$\{V_{12}\}$ (left) and $(PcLn)_2$-$\{V_{12}\}$ (right) representing different aggregation behavior. Distances close to 18 Å are considered as dimers. Some pairs form long-lived dimers during the whole trajectory, like POV1···POV4, whereas other pairs remain close for a while and then move away (as in case of POV1···POV7). Some POV units do not show aggregation, as shown in the two cases at the bottom. (D) Representative snapshots of PcLn-$\{V_{12}\}$ (top) and $(PcLn)_2$-$\{V_{12}\}$ (bottom), showing the most representative POV···POV interaction mode found. Color code: V = orange, Cl = green, Ln = turquois, N = blue, C = grey and H = white.

in time. The RDF is extracted from the averaged structural data of a dynamic system considering two reference points, typically atoms. Figure 7A shows the Cl···Cl RDF for four runs: diluted (5 mM) and concentrated (20 mM) CH_2Cl_2 solutions for each PcLn-$\{V_{12}\}$ and $(PcLn)_2$-$\{V_{12}\}$ compounds.

Upon inspection of the RDFs, we consider formation of a dimer if the distance between two Cl centers is less than the endpoint of the main peak of a RDF, namely 20 Å for PcLn-$\{V_{12}\}$ and 17.8 Å for $(PcLn)_2$-$\{V_{12}\}$. The RDFs for PcLn-$\{V_{12}\}$ (Figure 7A) present broad and not well-defined peaks around d(Cl-Cl) = 15 Å, suggesting the prevalence of monomeric units (86% and 77% for 5 and 20 mM, respectively (Figure 7B, left) over few short-lived dimers in solution. Conversely, the RDF of 20 mM solution of $(PcLn)_2$-$\{V_{12}\}$ displays a single sharp peak at *ca.* 16 Å, integrating to 0.83 molecules (Figure 7A, right). In the latter case, the formation of dimers is most preferable in the concentrated solution, accounting for 73% of the species (Figure 7B, right). In the dilute solution of $(PcLn)_2$-$\{V_{12}\}$ only monomers were observed.

In summary, the obtained MD simulation data indicate that the structural composition (one or two LnPc ligands *per* $\{V_{12}\}$ unit) and the concentration of the title nanocomposites determine their supramolecular behavior which, in turn, impacts their charge transfer characteristics in solution. Based on the experimental results of the concentration dependent EPR measurements (Figure 5) and the results of the MD calculations, we suggest that the reduction of the $\{V_{12}\}$ unit in solution takes place through *intra*molecular electron transfer from the Pc group to the $\{V_{12}\}$ core, initiated by sufficiently available *inter*molecular Pc···Pc contacts. These π–π dispersive interactions are hardly present, although not completely excludable, in the mono-substituted PcLn-$\{V_{12}\}$ characterized by the predominant degree of $\{V_{12}\}$···$\{V_{12}\}$ contacts that are mediated by the counter-cations.

DFT calculations

We applied the DFT as implemented in ADF2019[60,61] for the study of PcLn-$\{V_{12}\}$ and $(PcLn)_2$-$\{V_{12}\}$ nanocomposites with a combination of the following functionals: OPBE[62] for geometry optimizations and B3LYP[63,64] for the total energies and electronic structures of the equilibrium structures. The hydrogen-free, oxidized mono- and bis-substituted vanadium–oxo clusters were optimized for Ln = Gd (f^7) and Lu (f^{14}). The oxidized and the reduced forms of all Ln^{III} derivatives were computed adopting the *closest* reference lanthanide structure (Gd^{III} geometry for Ln = Sm^{III}, Eu^{III}, Tb^{III}, Dy^{III}, and Lu^{III} geometry for Ln = Er^{III}, Yb^{III}). Scalar relativistic corrections were introduced by means of the Zeroth-Order Regular Approximation (ZORA).[65–

[67] Triple-ζ + double polarization (TZ2P) basis sets with the frozen core approximation (C and N: 1s; Cl: 2s; V: 3p; Ln: 5p) were used. We also computed the metal-free phthalocyanine forms (the neutral (H_2Pc) and the deprotonated (Pc^{2-}) forms), the H-free $[V_{12}O_{32}Cl]^{5-}$ POV, and PcLnOAc. We applied the unrestricted formalism to all electronic open-shell systems, except for the oxidized Lu^{III}-containing systems, H_2Pc and $[V_{12}O_{32}Cl]^{5-}$. Organic solutions were mimicked with the Conductor-like Screening Model (COSMO).[68] We applied Mulliken's formula to obtain the atomic spin densities (ASD).

The fully oxidized $[V_{12}O_{32}Cl]^{5-}$ unit computed in solution, with all V^V metal centers, presents a rather large HOMO–LUMO gap of 3.9 eV. The highest occupied molecular orbital (HOMO) is found at –7.3 eV, with oxo nature, and the lowest unoccupied molecular orbital (LUMO) at –3.4 eV, with vanadium-like nature. If an extra electron is added to the system, it is delocalized equally over 8 vanadium centers. The H_2Pc molecule, slightly bent (C_{2v}), is featured by a HOMO–LUMO gap of 2.3 eV, marginally larger than that observed for the planar (D_{4h}) Pc^{2-} (2.1 eV). The calculations in acetonitrile solution resulted in HOMOs at –5.2 eV and –4.4 eV for H_2Pc and Pc^{2-}, respectively. Hence, the LUMO of $\{V_{12}\}$ is higher in energy than the HOMO of Pc. The hydrogen-free forms of $(PcLn)_n$-$\{V_{12}\}$, with charges –4 (n = 1) and –3 (n = 2), were computed applying maximal M_s values with all-parallel spins. Frontier orbital energies are shown in Figure 8 for mono- and bis-substituted Yb^{III}-based systems each in the oxidized and the reduced forms. The general molecular features regarding the electronic structure in terms of molecular orbitals are discussed taking the DFT results for Ln = Yb. This choice is practically irrelevant since there is almost no dependence on the Ln. In other parts of this section, in which the Ln influences the characteristics of the systems, it is clearly stated.

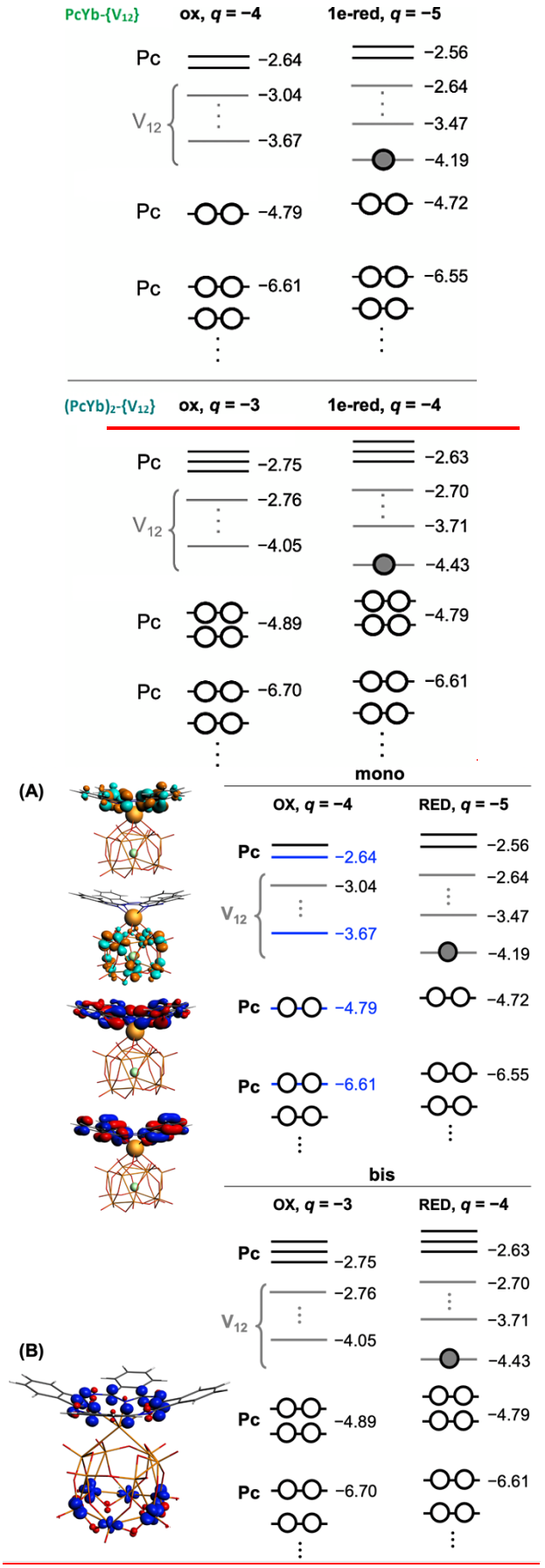

Figure 8. DFT analysis of the electronic structure of the mono- and bis-substituted $(PcLn)_n$-$\{V_{12}\}$ compounds. (A) Sequence of energies (in eV) and occupations of the frontier MOs for PcYb-$\{V_{12}\}$ (top) and $(PcYb)_2$-$\{V_{12}\}$ (bottom) in their oxidized (OX) and one electron reduced (RED) forms. The character of the orbitals is labeled. Circles represent electrons. Selected MOs of the oxidized mono form (corresponding to the horizontal blue lines) are represented. The rest of the orbitals in the V_{12} block are also vanadium-3d combinations, with similar nature to the orbital depicted. (B) Spin density of the charge-separated mono species, $(PcLu)^{\bullet+}$-$\{V^{IV}V^{V}_{11}\}$. Blue and red lobes denote regions with the up and down net spin, respectively. ~~Sequence of energies and occupations of the frontier MOs, for the mono-substituted PcYb-$\{V_{12}\}$ (top) and the bis-substituted $(PcYb)_2$-$\{V_{12}\}$ (bottom) in their oxidized (ox) and one-electron reduced (1e-red) forms. Counter-cations were not part of these calculations. Circles represent electrons. Values are given in eV.~~

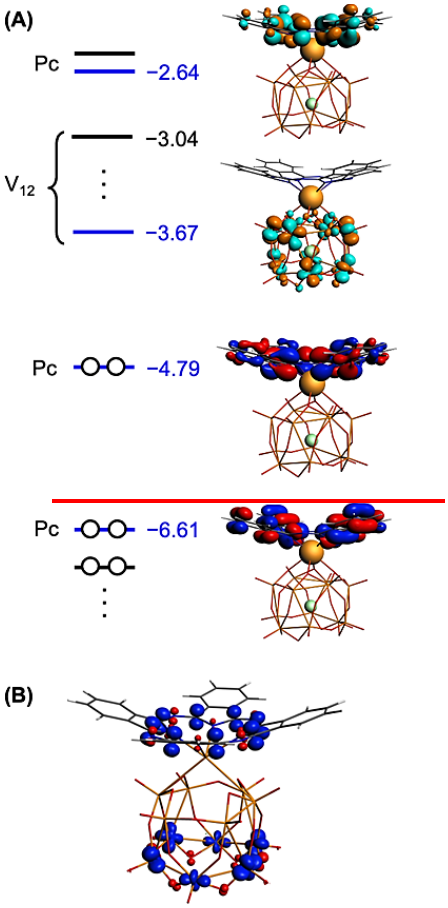

~~**Figure 9.** DFT analysis of the electronic structure of the mono-substituted PcLn-$\{V_{12}\}$ compounds. (A) Representation of selected MOs (corresponding to the horizontal blue lines) in the oxidized form of PcYb-$\{V_{12}\}$. The character of the orbitals is shown. The rest of the orbitals in the V_{12} block are also vanadium-3d combinations, with the same nature as the orbital depicted. (B) Spin density of the charge-separated species $(PcLu)^{\bullet+}$-$\{V^{IV}V^{V}_{11}\}$. Blue and red lobes denote regions with the up and down net spin, respectively.~~

Any mono-substituted system presents a HOMO with Pc nature at *ca.* –4.8 eV, irrespective of Ln, while the LUMO with $\{V_{12}\}$ nature lies 1.1 eV above in all cases (Figure 9A for the representation of the selected MOs).

ASD values obtained for oxidized complexes confirm that the unpaired electrons are fully located on Ln with 6.99 for Gd^{III} (f^7), 6.01 for Eu^{III} (f^6) and 5.00 for Sm^{III} (f^5), whereas other atoms present net zero values.

Table 2. ASD values computed for the mono-substituted PcYb-$\{V_{12}\}$ and the bis-substituted $(PcYb)_2$-$\{V_{12}\}$ each in the oxidized (OX~~ox~~) and one-electron reduced (~~1e-red~~RED) forms. For PcLu-$\{V_{12}\}$, the charge-separated (CS) state ASDs are listed (see also Figure ~~8~~9B).

compound	region	~~ox~~OX	~~1e-re-d~~RED	Lu^{III} CS
PcLn-$\{V_{12}\}$	Yb	0.995	0.995	0.0
	$\{V_{12}\}$	0.0	0.294 (×2) 0.282 (×2) 0.148 (×2)	0.295 (×2) 0.282 (×2) 0.146 (×2)
	Pc	0.0	0.0	0.144 (×8)
$(PcLn)_2$-$\{V_{12}\}$	Yb	0.985 (×2)	0.987 (×2)	-
	$\{V_{12}\}$	0.0	0.174 (×8)	-
	Pc	0.0	0.0	-

~~Any mono-substituted system presents a HOMO with Pc nature at *ca.* –4.8 eV, irrespective of Ln, while the LUMO with $\{V_{12}\}$ nature lies 1.1 eV above in all cases (Figure 9A for the representation of the selected MOs).~~

~~ASD values obtained for oxidized complexes confirm that the unpaired electrons are fully located on Ln with 6.99 for Gd^{III} (f^7), 6.01 for Eu^{III} (f^6) and 5.00 for Sm^{III} (f^5), whereas other atoms present net zero values.~~

The bis-substituted representatives are featured by similar ASD values for Ln centers. Regarding one-electron reduced systems, when the extra electron added is parallel to the net spin of Ln, in mono-substituted compounds the additional electron occupies the orbital delocalized over six vanadium centers at –4.2 eV (see the ASDs in Table 2), whereas the spin populations of the Ln centers remain unchanged. The behavior of the bis-substituted derivatives is similar – the additional electron is equally delocalized over eight vanadium centers that participate in the orbital at –4.4 eV. In 1e-reduced systems, when the extra electron located on $\{V_{12}\}$ is forced to have the opposite spin with respect to that of the Ln center(s) leads to computed ASD absolute values identical to those of the all spin-up 1e-reduced systems. The energy differences between the all spin-up (HS) and the *spin-flipped* (LS) solutions are usually small, below ~2 cm^{-1} (< $3\cdot10^{-4}$ eV), except for the mono-substituted Eu^{III}- and Yb^{III}-based systems (with HS ~60 cm^{-1} and ~220 cm^{-1} lower than LS, respectively) and the bis-substituted Dy^{III}-based system (LS is ~13 cm^{-1} lower than HS), suggesting that the net spins in the $\{V_{12}\}$ and Ln regions are mostly uncoupled.

For the investigation of the *intra*molecular Pc → $\{V_{12}\}$ electron transfer in mono-substituted PcLn-$\{V_{12}\}$ compounds, we computed the electronic spectra of Ln = Dy^{III}, Lu^{III} and Gd^{III} to obtain a strong transition involving molecular orbitals of either

part of the molecule. Such *intra*molecular electronic transitions, at this level of computation, are described only qualitatively. For each system, we computed the lowest 20 allowed purely electronic transitions. Interestingly, for the Dy^{III}-based system no Pc → $\{V_{12}\}$ electron transitions were obtained, which roughly corresponds to the experimental observation of one of the weakest V^{IV} signals in EPR for Dy^{III}-containing systems. A weak electron transition in the IR range (1320 nm) was computed for the Lu^{III}-based system, whereas the Gd^{III}-based mono-substituted compound presents the strongest one at *ca.* 620-630 nm with the oscillator strengths *ca.* 100 times larger than for the Lu^{III} analogue. These results suggest that, even not considering the vibronic coupling, there is a non-negligible probability of *intra*molecular electron transfer, at least when Gd^{III} and Lu^{III} are involved. Figure 8~~9~~B represents the calculated spin density of the charge-separated mono-$(PcLu)^{\bullet+}$-$\{V^{IV}V^{V}_{11}\}$ which, formally, results from the *intra*molecular charge transfer process.

The *inter*molecular electron mobility in PcLn-$\{V_{12}\}$ and $(PcLn)_2$-$\{V_{12}\}$ compounds was investigated using the TRANSFERINTEGRALS feature in ADF package.[61] The values reported herein were obtained from different structural arrangements (crystallographic coordinates, MD snapshots of solution simulations) and single point DFT calculations.

The analysis of the unit cell packing of PcY-$\{V_{12}\}$ leads to the assumption that two electron-hopping pathways are possible, namely one *vertical* and one *transversal*. Ideally, the vertical pathway is a two-step process: 1) the electron transfer from the PcY-$\{V_{12}\}$ anion to nBu$_4$N$^+$ followed by 2) the electron transfer from the resulted formally neutral nBu$_4$N species to another PcY-$\{V_{12}\}$ anion (see Figure 9~~10~~). For the vertical electron-hopping pathway we calculated $|J_{eff}^1|$ = 0.0164 eV for the first step and $|J_{eff}^2|$ = 0.0141 eV for the second step. On the other hand, the transversal pathway assumes a direct electron transfer from one PcY-$\{V_{12}\}$ unit to another PcY-$\{V_{12}\}$ without the mediation by counter-cations due to the proximity between two neighboring units. We computed a very small value of $|J_{eff}|$ = 0.00021 eV, suggesting that the transversal pathway is improbable and, therefore, was not taken into consideration by computing MD arrangements given a rather small impact of aggregation. The electronic structure of the electron deficient mono-$[(PcY)^{\bullet+}$-$\{V_{12}\}]^{3-}$ compound, generated upon electron hopping from Pc to a neighboring molecule, is represented in Figure S64.

~~The mechanistic considerations of electron hopping in bis-derivatives made from the analysis of the cell packing in $(PcDy)_2$-$\{V_{12}\}$ are similar to those of mono-substituted analogues. Here, electron transfer takes place from a Pc group of one molecule to the closest nBu$_4$N$^+$ cation, and right away to the next Pc moiety of another molecule involving, again, intercurrent neutral nBu$_4$N$^\bullet$ species (Figure S65). The estimated *effective transfer integrals* of $|J_{eff}^1|$ = 0.00432 eV and $|J_{eff}^2|$ = 0.00446 eV were obtained at the DFT level for Ln = Lu. These are considerably smaller than those for the mono-substituted system and might be attributed *inter alia* to the cell packing differences between the corresponding crystal systems and therewith related proximity of the units to each other. The calculation of a direct *inter*molecular electron hopping, namely without any kind of mediation *via* counter-cations, between the two Pc units for a 20 mM concentrated solution of the bis-derivative resulted in a rather large *effective transfer integral* $|J_{eff}|$ = 0.0136 eV, which roughly explains the experimentally observed strong EPR signal assigned to V^{IV}.~~

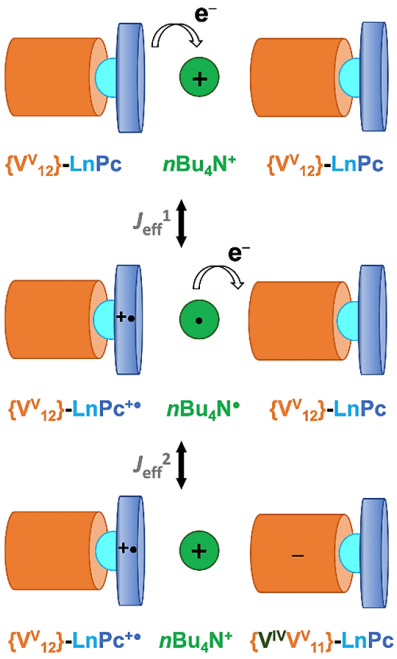

Figure 9~~10~~. Counter-cation mediated *inter*molecular electron transport process for mono-PcLn-$\{V_{12}\}$ compounds, as present at high sample concentrations. Only a section is represented for clarity, not showing additional nBu$_4$N$^+$ counter-cations and H^+. The process involves hopping of one electron from a Pc moiety of one PcLn-$\{V_{12}\}$ anion to the $\{V_{12}\}$ moiety of another PcLn-$\{V_{12}\}$ anion, with the nBu$_4$N$^+$ / nBu$_4$N$^\bullet$ pair as a charge mediating platform.

The mechanistic considerations of electron hopping in bis-derivatives made from the analysis of the cell packing in $(PcDy)_2$-$\{V_{12}\}$ are similar to those of mono-substituted analogues. Here, electron transfer takes place from a Pc group of one molecule to the closest nBu$_4$N$^+$ cation, and right away to the next Pc moiety of another molecule involving, again, intercurrent neutral nBu$_4$N$^\bullet$ species (Figure S65). The estimated *effective transfer integrals* of $|J_{eff}^1|$ = 0.00432 eV and $|J_{eff}^2|$ = 0.00446 eV were obtained at the DFT level for Ln = Lu. These are considerably smaller than those for the mono-substituted system and might be attributed *inter alia* to the cell packing differences between the corresponding crystal systems and therewith related proximity of the units to each other. The calculation of a direct *inter*molecular electron hopping, namely without any kind of mediation *via* counter-cations, between the two Pc units for a 20 mM concentrated solution of the bis-derivative resulted in a rather large *effective transfer integral* $|J_{eff}|$ = 0.0136 eV, which roughly explains the experimentally observed strong EPR signal assigned to V^{IV}.

Photo- and radiation chemical study

Further insights into the nanocomposite with the charge-separated $(PcLu)^{\bullet+}$-$\{V^{IV}V^{V}_{11}\}$ states as suggested by DFT (Figure 8B~~9~~) were gained by laser photolysis transient absorption spectroscopy. Photo- and radiation chemical studies of the electron donor–acceptor nanocomposites PcLu-$\{V_{12}\}$ and $(PcLu)_2$-$\{V_{12}\}$ as well as the reference compounds $\{V_{12}\}$ and PcLuOAc were conducted in solution to investigate possible photoinduced electron transfer reactions between the photoexcited PcLn group and the $\{V_{12}\}$ cage. With the notion that $\{V_{12}\}$ may act as electron acceptor in PcLu-$\{V_{12}\}$ and $(PcLu)_2$-$\{V_{12}\}$, the one-

electron reduction of $\{V_{12}\}$ by solvated electrons in aqueous solutions was probed. Such conditions necessitate the radiolysis of nitrogen saturated dilute aqueous $\{V_{12}\}$ solutions containing 5 vol% *tert*-butanol. The radiolysis of water lead to the production of three highly reactive species, namely $^{\bullet}H$, $^{\bullet}OH$, and e_{aq}^- (equation (1)), besides the molecular products H_2 and H_2O_2.[69] The function of *t*-butanol is to efficiently scavenge two of the radical species, namely $^{\bullet}H$ and $^{\bullet}OH$, via hydrogen abstraction (equation (2))[69] so that only e_{aq}^- – a very strong reducing intermediate[70] – remains as reactive species to react with $\{V_{12}\}$, forming the one-electron reduced form of the $\{V_{12}\}$ (equation (3)).

$$H_2O \rightsquigarrow e^-_{aq} + {}^{\bullet}H + {}^{\bullet}OH \quad (1)$$

$$(CH_3)_3COH + {}^{\bullet}OH\,({}^{\bullet}H) \rightarrow {}^{\bullet}CH_2(CH_3)_2COH + H_2O\,(H_2) \quad (2)$$

$$\{V_{12}\} + e_{aq}^- \rightarrow \{V_{12}\}^- \quad (3)$$

Immediately after the radiation pulse, a well-established broad transient absorption of e_{aq}^- with its maximum at around 720 nm was recorded, which decayed rapidly in the presence of $\{V_{12}\}$ giving rise to a new transient throughout the UV and visible part of the optical spectrum. Features of the resulting absorption spectrum (Figure S66) include a maximum at 350 nm and a minimum at 310 nm which can be assigned to the one-electron reduced $\{V^{IV}V^{V}_{11}\}$ cage. The rate constant for the reaction of the fully-oxidized $\{V^{V}_{12}\}$ with e_{aq}^- was determined from the decay of the transient absorption of e_{aq}^- at 720 nm at different $\{V_{12}\}$ concentrations (Figure S66) assuming a pseudo-first-order kinetic. In this way a bimolecular rate constant with the value of 5×10^9 $M^{-1}s^{-1}$ was obtained. With the transient absorption spectrum of the one-electron reduced $\{V^{IV}V^{V}_{11}\}$ on hands, photophysical studies of PcLuOAc, PcLu-$\{V_{12}\}$ and $(PcLu)_2$-$\{V_{12}\}$ were conducted.

The electronic ground state absorption spectrum of PcLuOAc exhibits a set of Q-bands, an intense absorption maximum at around 673 nm preceded by a minor maximum at around 610 nm. Additionally, B-band (the Soret-bands) absorptions of the Pc macrocycle are observed at around 342 nm (Figure 10~~1~~). The observation of the Q- and B-band absorptions are in line with the plethora of the published absorption spectra typical for metal phthalocyanines.[71,72]

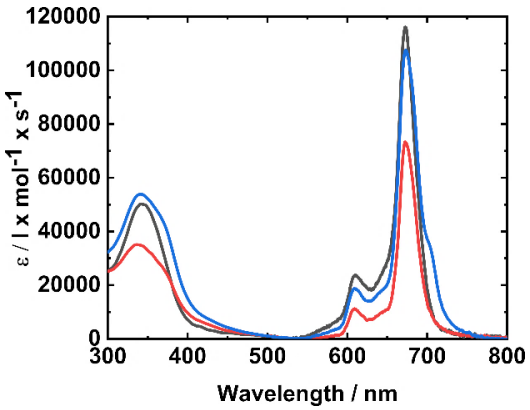

Figure 10~~1~~. Absorption spectra of PcLuOAc in toluene (black), PcLu-$\{V_{12}\}$ in THF (red) and $(PcLu)_2$-$\{V_{12}\}$ in THF (blue).

Upon the comparison of the electronic ground state absorptions of the electron donor–acceptor PcLu-$\{V_{12}\}$ and $(PcLu)_2$-$\{V_{12}\}$ with that of PcLuOAc, the two nanocomposites can be qualitatively described as the sum of the absorption spectra of PcLuOAc and $\{V_{12}\}$. In particular, strong Q-bands with absorption maxima at around 673 nm and 609 nm accompanied by the B-band absorptions with maxima at 335 nm (PcLu-$\{V_{12}\}$) and 339 nm ($(PcLu)_2$-$\{V_{12}\}$) based on the phthalocyanine-centered transitions were observed (Figure 10~~1~~). Interestingly, the absorption spectrum of $(PcLu)_2$-$\{V_{12}\}$ shows a shoulder at the low energy edge of the Q-band absorption around 710 nm. The nature of the shoulder may relate to a charge transfer band, on the one hand;[73] on the other, the formation of aggregates showing similar spectroscopic features cannot be excluded either.[74,75] The lower extinction coefficients of the Q-band for PcLu-$\{V_{12}\}$ and $(PcLn)_2$-$\{V_{12}\}$ compared to PcLuOAc may indicate electronic communication between the PcLu and $\{V_{12}\}$ moieties in the ground state, which was previously observed for different porphyrinoid-based electron donor–acceptor systems.[76–78] The B-band absorptions of PcLu-$\{V_{12}\}$ and $(PcLu)_2$-$\{V_{12}\}$ appear somewhat broader than that observed for PcLuOAc and the maxima are slightly shifted towards the UV area. The most feasible rationale for this finding is that the UV absorption of PcLu-$\{V_{12}\}$ and $(PcLu)_2$-$\{V_{12}\}$ can be described as an overlap of the B-band absorption of the phthalocyanine macrocycle with the absorption spectrum of $\{V_{12}\}$; the latter is characterized by the absorption mainly in the UV region of the optical spectrum with a maximum at around 232 nm and a shoulder at around 340 nm (Figure S67).

The excited state properties of PcLuOAc, PcLu-$\{V_{12}\}$ and $(PcLu)_2$-$\{V_{12}\}$ were studied by fluorescence and nanosecond laser photolysis transient absorption spectroscopy. LuPcOAc in toluene, PcLu-$\{V_{12}\}$ and $(PcLu)_2$-$\{V_{12}\}$, both in tetrahydrofurane (THF), exhibit only marginal fluorescence with maxima at around 680, 672 and 673 nm (Figure S68) and quantum yields of 0.0035, 0.0032 and 0.0027, respectively.[§] In line with the very low fluorescence quantum yields, fluorescence lifetime measurements for all three compounds revealed lifetimes below the resolution of our TCSPC setup (below 100 ps) indicating that the first excited singlet state lifetime for PcLuOAc, PcLu-$\{V_{12}\}$ and $(PcLu)_2$-$\{V_{12}\}$ lay below 100 ps.

The transient absorption signature of the first excited triplet state of PcLuOAc was established by means of the nanosecond laser photolysis. It consists of a broad transient absorption maximum at around 490 nm accompanied by transient absorption minima at 340, 610 and 670 nm mirror-imaging the B- and Q-bands of the ground state absorption (Figure S69). This transient absorption is in line with previously reported transition absorptions of the T_1 state of phthalocyanine macrocycles.[71,79,80] To shed light on a possibly formed charge-separated state in $(PcLu)^{\bullet+}$-$\{V^{IV}V^{V}_{11}\}$ and $(PcLu)_2^{\bullet+}$-$\{V^{IV}V^{V}_{11}\}$, nanosecond-resolved transient absorption spectroscopy was employed. Hereby, PcLu-$\{V_{12}\}$ and $(PcLu)_2$-$\{V_{12}\}$ were probed in THF upon photoexcitation at 355 nm.

The transient absorption spectrum (Figure 11~~2~~) obtained from PcLu-$\{V_{12}\}$ shows absorption bands throughout the visible and NIR part of the optical spectrum with a broad maximum at around 550 nm and a rather narrow maximum at around 830 nm. Such transient absorptions, in particular the transient absorption maximum around 830 nm, is diagnostic for one electron oxidized phthalocyanine radical cations,[81–84] giving strong evidence for the envisioned electron transfer from the photoexcited PcLu ligand to the $\{V_{12}\}$ cage in PcLu-$\{V_{12}\}$. Fitting the decay at 830 nm (Figure 11~~2~~, inset) with a monoexponential decay function resulted in lifetimes for the $(PcLu)^{\bullet+}$-$\{V^{IV}V^{V}_{11}\}$ state of around 170 ns, which is rather long lived taking the close proximity of the electron donor and acceptor into account.

For $(PcLu)_2$-$\{V_{12}\}$ the obtained transient absorption spectrum differs considerably from that of PcLu-$\{V_{12}\}$. Photoexcitation of $(PcLu)_2$-$\{V_{12}\}$ in THF with nanosecond laser pulse at 355 nm resulted in strong transient absorptions throughout the UV and a visible part of the optical spectrum with maxima at around 620 and 830 nm and a minimum at around 690 nm. This transient absorption decayed rather rapidly with a lifetime of around 40 ns (Figure S70). The observed transient absorption resembles neither the transient absorption spectrum of the T_1 state of PcLuOAc nor the commonly seen transient absorption signatures of the one electron oxidized phthalocyanine macrocycles. This observation can probably be explained by the fact that in $(PcLu)_2$-$\{V_{12}\}$ the $\{V_{12}\}$ unit is sandwiched between the two PcLu fragments, and therefore, an electron transfer to $\{V_{12}\}$ may result in a distribution of the positive charge between both PcLu moieties, thus leading to a transient absorption spectrum not fitting with the absorption spectrum of a one-electron oxidized Pc macrocycle.

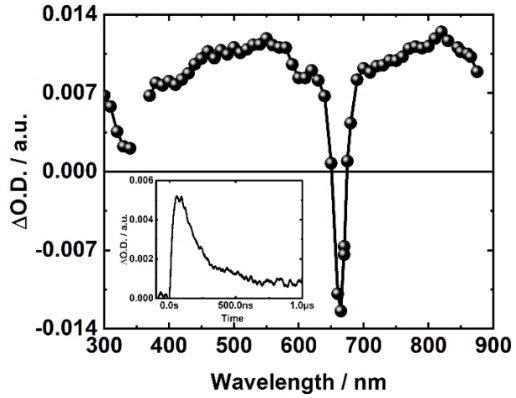

Figure 11~~2~~. Nanosecond laser photolysis transient absorption spectrum of PcLu-$\{V_{12}\}$ in N_2 saturated THF 150 ns after excitation at 355 nm (5 ns FWHM, 5 mJ/pulse). Inset: Corresponding time absorption profiles at 830 nm.

Magnetism and magnetochemical modelling

To gain preliminary insights into the opportunities to utilize the synthesized molecular nanocomposites with Ln = Sm^{III}–Er^{III} and Lu^{III} as information storage,[85–88] we measured AC susceptibility. Only the Dy^{III}-containing mono- and bis-derivatives revealed some non-zero out-of-phase signal. In the following magnetochemical studies we focus exclusively on the PcDy-$\{V_{12}\}$ derivative as it has the strongest AC magnetism.

Both DC and AC measurements have been performed by the standard SQUID technique (B = 0–7.0 T and T = 2.0–300.0 K, f = 1–1200 Hz, for further details of the measurements refer to the ESI[†]). The EPR (Figure 4) revealed that the magnetism of PcDy-$\{V_{12}\}$ is induced not only by Dy^{III} but also by an electron delocalized over $\{V_{12}\}$. However, DFT results exclude a possibility of an electron transition from Pc to $\{V_{12}\}$. Thus, it seems that in this compound we observe *inter*molecular charge transfer from Pc to $\{V_{12}\}$ (*via* counter-cations) resulting in two configurations: one-electron reduced (Figure 8) and electron deficient (Figure S64). The latter one cannot be detected by room temperature EPR.[40] In both configurations there is an extra electron that can interact with Dy^{III}. Therefore, under the assumption that below room temperature only the ground multiplet arising from spin-orbit coupling (in Dy^{III}) is relevant, the DC magnetic measurements can be modelled by the following Hamiltonian (equation (4)):

$$H = -\mu_B\left[g_\perp\left(J_xB_x + J_yB_y\right) + g_\parallel J_zB_z + g\boldsymbol{S}\cdot\boldsymbol{B}\right] + K\boldsymbol{S}\cdot\boldsymbol{J} + DJ_z^2 + E\left(J_x^2 - J_y^2\right), \quad (4)$$

where $\boldsymbol{J} = (J_x, J_y, J_z)$ (J = 15/2) is the total angular momentum of Dy^{III} and $\boldsymbol{S}$ is the spin ½ of an electron delocalized over some ions at $\{V_{12}\}$, or at Pc. The last two terms account for the interaction of $\boldsymbol{J}$ with the crystal field. The z-axis goes through Cl^- and Dy^{III} ions. First, we assumed that $E = 0$. Then, the best fit (fit a) has been obtained for $g_\perp = 1.30$, $g_\parallel = 1.34$, $K/k_B = 1.7\ K$, $D/k_B = -12.2\ K$ (Figure 1~~2~~3). Since the fitted g values are very close to the free ion $g = 4/3$ one can eliminate g from the fitting by fixing it to the free ion value and obtain very similar unique values of D and K (Figure S71). Yet, the introduction of small anisotropy in g allows to fine tune the fit in high temperatures. Moreover, it can be demonstrated that a condition $K \neq 0$ is indispensable to obtain a good fit and cannot be substituted by more crystal field terms (Figure S71), which clearly indicates existence of the interaction between Dy^{III} and the radical electron. (see the Supporting Information for the detailed DC modelling). The observed room temperature χT was found to be $1.78{\cdot}10^{-4}$ m^3 mol^{-1}, which is within the range for a theoretical value of $1.77{\cdot}10^{-4}$ m^3 mol^{-1} for a free Dy^{III} ion and $1.81{\cdot}10^{-4}$ m^3 mol^{-1} when an additional electron is considered. A weak antiferromagnetic interaction $K/k_B = 1.7$ K between the Dy^{III} ion and the unpaired electron is stronger than the above DFT estimate (< 0.46 K). It can be due to the fact that the DFT estimate is only true for the interaction between Dy^{III} and $\{V_{12}\}$-delocalized electron whereas the value obtained from the fitting is an average of interaction of Dy^{III} with Pc- and $\{V_{12}\}$-located electrons.

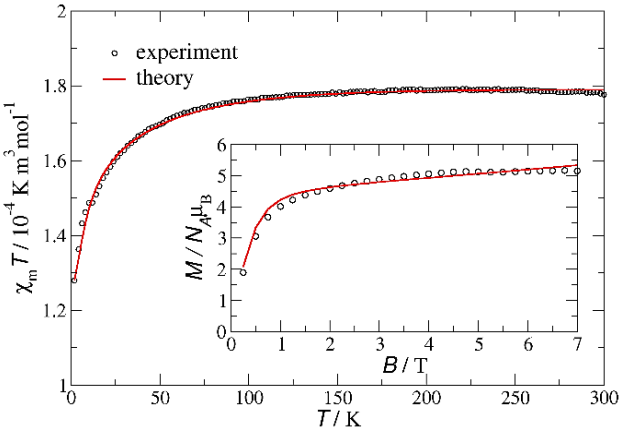

Figure 12~~3~~. Molar susceptibility (B = 0.1 T) and magnetization (T = 2 K) for PcDy-$\{V_{12}\}$ (black circles) with theoretical fits assuming E = 0 (solid red lines).

The negative D value suggests the existence of an energy barrier in the Orbach relaxation process estimated to be around 686 K. However, in the absence of the static field the AC out-of-phase signal at temperatures below 10 K shows no clear peaks in the available frequency range. This points out a fast relaxation through quantum tunnelling of magnetization (QTM).[89,90]

When the static field is applied the AC out-of-phase signal exhibits clear peaks. Using standard methods[91] (see also the Supporting Information) we extracted the relaxation time from measurements made at T = 2 K for different static fields B. The best fit for the relaxation rate τ^{-1} versus B was obtained with

the equation (5) considering QTM and direct paths of relaxation[92] (Figure 134):

$$\tau^{-1} = \frac{b_1}{1+b_2B^2} + aTB^n, \quad (5)$$

with the following parameters: $b_1 = 17133 \pm 2765$ 1/s, $b_2 = 1695 \pm 302$ 1/T^2, a = 32296 ±22235 T^{-n}/Ks, n = 5.08 ±0.6 and B in Tesla. The uncertainties (given after ±) define 95% confidence intervals. For $B = 0$ the relaxation rate of PcDy-{V_{12}} has a divergent error bar (with the upper limit against the infinity) indicating that the relaxation time cannot be measured with the current method.

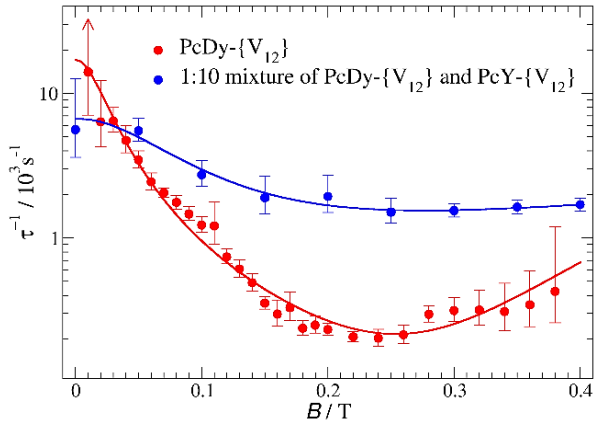

Figure ~~14~~13. Relaxation rate for different values of the static field B at T = 2 K obtained for PcDy-{V_{12}}. The fitting has been performed based on the formula (5). The error bars mark 95% confidence intervals.

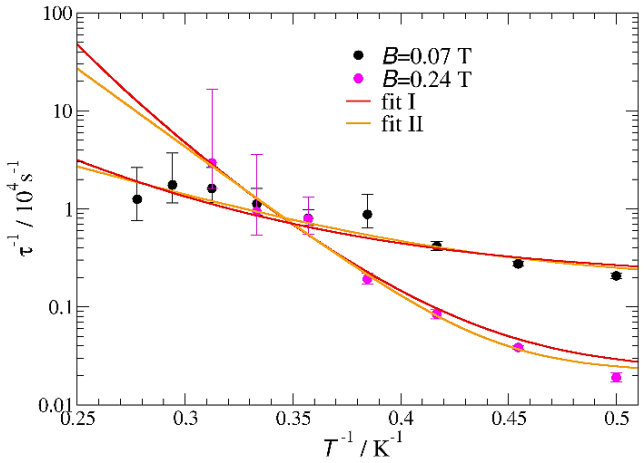

Figure 1~~4~~5. Temperature dependence of relaxation rate for static field $B = 0.07$ T and $B = 0.24$ T in PcDy-{V_{12}}. The error bars mark 95% confidence intervals.

Temperature dependent measurements were performed for B = 0.07 T and B = 0.24 T, for which the strongest out-of-phase signal and the longest relaxation time (at T = 2 K) were found, respectively (Figures S72-S78). In Figure 1~~5~~4 the relaxation rate is plotted versus temperature. For temperatures higher than 3.6 K the relaxation time is too short and cannot be detected with a standard AC magnetometry. The following two approaches gave equally good results: I) fitting the data with QTM, direct and Raman processes (the first three terms in equation (6)), and II) fitting the data with QTM, direct and Orbach processes (the first, second and fourth term in equation (6)):

$$\tau^{-1} = \tau_{QTM}^{-1} + aTB^n + CT^m + \exp\left(-\frac{E_{eff}}{T}\right)/\tau_0, \quad (6)$$

where τ_{QTM}^{-1} is the first term in formula (5) calculated for the given field.

Table 3. Fitted parameters in equation (6) and their 95% confidence intervals (in square brackets). Confidence intervals are due to error bars of τ^{-1} and to uncertainties of τ_{QTM}^{-1} , a and n obtained from the fit of formula (5).

fit	parameters	B = 0.07 T	B = 0.24 T
I	C / sK^{-m}	23.1 [4.4, 53.5]	0.012 [0.003, 0.02]
	m	5.16 [4.5, 6.4]	12.64 [12.1, 13.7]
II	E_{eff} / K	14.5 [12.6, 18]	36.8 [34.6, 39.4]
	τ_0 / 10^{-6}s	1 [0.52, 1.6]	3.7 [2.2, 5.2] · 10^{-4}

Parameters a and n attain the values according to equation (5). For B = 0.07 T a direct process has negligible contribution to τ^{-1} and is omitted in fitting. The remaining parameters in (6) are obtained from the fitting of τ^{-1} versus T and are shown in Table 3. Attempts to fit τ^{-1} versus T with the formula containing QTM, Raman, and Orbach processes simultaneously or in other combinations were unsuccessful. In Kramers doublet systems like Dy^{III} QTM is formally forbidden.[93] However, in real systems the time reversal symmetry is often broken by the transverse local magnetic fields resulting from the dipole magnetic interaction with other magnetic molecules[94] or the interaction with magnetically active nuclei[95] thus opening a tunnel splitting. The transverse crystal field can influence the size of a tunnelling gap.[96] In the case of the PcDy-{V_{12}} compound there is additionally an interaction with the unpaired electron delocalized over {V_{12}} cluster. All these factors may play a role in encouraging relaxation through QTM.

To verify the impact of the magnetic dipole interactions between Dy^{III} ions we determined the relaxation rate in 1:10 mixture of PcDy-{V_{12}} and PcY-{V_{12}} (Figure 13) at T = 2 K. As Y^{III} is diamagnetic, the distance between Dy^{III} ions and thus the strength of magnetic dipole interactions should decrease. Indeed, at B = 0 the relaxation rate assumes a finite value. Yet, the relaxation time at B = 0 is still short suggesting that other factors can also play a role. It can be shown, for instance, that the strength of the magnetic dipole interaction between Dy^{III} ion and an electron at {V_{12}} is of the same order as the strength of the same interaction between Dy^{III} ions (see the Supporting Information).

In ~~T~~the energy spectrum of Hamiltonian (4) with optimal parameters ~~is~~ (presented in Figure S80)~~16~~ t. ~~T~~he eigenstates have a form of a superposition of states $|m_J\rangle|m_S\rangle$, where m_J and m_S stand for the projections of $\boldsymbol{J}$ and $\boldsymbol{S}$, respectively. ~~The lines marking the energy levels in Figure 16 extend over the values of m_J (labelled at the horizontal axis) which correspond to the components $|m_J\rangle$ presented in a superposition forming a given eigenstate.~~ Obviously, the interaction with the unpaired electron at {V_{12}} or Pc~~)~~ leads to the splitting of all energy levels and the superposition of the states with different projections m_J. The energy gap between the ground and the first excited states is equal to 13.1 K (13.8 K, if magnetic dipolar interactions are considered), which fits well to the effective energy barrier obtained

from the fitting of the QTM, and Orbach processes (12.6–18. K) for $B = 0.07$ T.

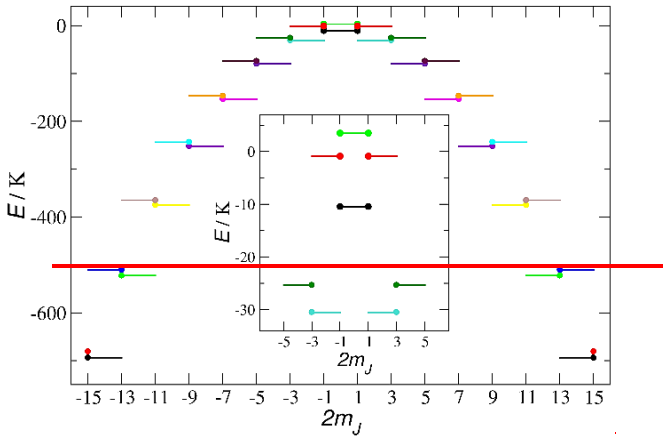

~~**Figure 16.** Energy spectrum of PcDy-{V_{12}} for static field $B = 0$. The lines marking energy levels extend over m_J represented in an eigenstate. Circles mark dominant components and the states from the same doublet are plotted with the same color.~~

This may indicate that for $B = 0.07$ T the thermally assisted QTM process takes place through the first excited state, which will favor the fit II. For $B = 0.24$ T it is difficult to find a correspondence between the energy spectrum and the effective energy (34.6–39.4 K) obtained from the fit II. This may be caused by a large magnitude of the external magnetic field, which hinders the thermally assisted QTM through the first excited state. Therefore, in this case the fit I, which considers a Raman process, should be favored. When the magnetic dipolar interaction between Dy^{III} ion and the electron at {V_{12}} is included in Hamiltonian (4) the optimal parameters are slightly different and the energy spectrum looks very much the same as that presented in Figure S80~~16~~ with the major differences being that the doublets are not degenerated anymore, and the eigenstates contain a superposition of states with all possible m_J. The tunnel splitting is equal to $1.26 \cdot 10^{-8}$ K for the lowest doublet and $1.6 \cdot 10^{-6}$ K for the first excited doublet.

In principle, these results support the idea of QTM through the ground and first excited states. However, in the low lying states the superposition of terms with opposite values of m_J is very small. For instance, in the ground doublet the dominant component corresponding to $m_J = -15/2$ or $15/2$ has a 99.97% share in the eigenstate. Thus, a direct tunnelling between these states is unlikely and there must be another mechanism that introduces larger superposition of states with opposite m_J. Such a superposition can be induced by e.g., transverse crystal field terms. To test this possibility, we introduced to the Hamiltonian (4) the lowest order transverse crystal field term. Since $g_\perp$ and $g_\parallel$ from the optimal fit (fit a) are very close to each other we fix $g_\perp = g_\parallel$. Then, starting from the optimal fit a, we found an almost equally good fit (fit b) with nonzero value of E: $g_\perp = g_\parallel = 1.33$, $K/k_B = 1.6$ K, $D/k_B = -9$ K, $E/k_B = 2.6$ K. The low-lying energy spectrum is very similar to that in fit a, but there is a large superposition of the terms with the opposite values of m_J. For example, the contributions of the terms with $m_J = 15/2$ and $m_J = -15/2$ in the split ground doublet are approximately equal to 49%. The tunnel splitting is equal to $1.6 \cdot 10^{-4}$ K for the ground doublet and $3.2 \cdot 10^{-5}$ K for the first excited doublet. Of course, the fitting of susceptibility does not enable us to determine more than a leading crystal field term. Therefore, fit b should be considered only as a proof of concept.

Thus, it can be concluded that the pure QTM relaxation at 2 K is probably enhanced at higher temperatures by thermally assisted QTM (for smaller magnetic fields) or Raman processes (for larger magnetic fields). The QTM cannot be completely quenched by dilution with non-magnetic molecules because tunnel splitting of doublets is caused also by the magnetic dipolar interaction between Dy^{III} ion and an electron at {V_{12}} or Pc and probably also enhanced by transverse crystal field terms.

CONCLUSIONS

We successfully synthesized and fully characterized a series of mono- and bis-functionalized nanocomposites PcLn-{V_{12}} and $(PcLn)_2$-{V_{12}}, respectively. Solution and solid state EPR revealed that proximity of the molecules generates reduced V(3d) states in the closely packed {$V_{12}O_{32}$} cages. As corroborated by a combined experimental and computational approach this effect can be assigned to two processes:

1) a non-photoinduced *intra*molecular electron transfer from the electron-donating LnPc moiety to the electron-accepting redox-active {$V_{12}O_{32}$} building block of the nanocomposite with the resulting charge-separated states $(PcLn)^{\bullet+}$-{$V^{IV}V^{V}_{11}$}. This process can be exemplified in Lu-based mono compound, where a radical electron located also at Pc is confirmed by r.t. EPR. The existence of the charge-separated state is confirmed by laser photolysis transient absorption spectroscopy. DFT calculations provide a nonzero probability of the electron transition from Pc to {V_{12}}. *Intra*molecular charge transfer seems to be excluded for the Dy-based mono compound as no Pc $\rightarrow$ {V_{12}} transitions were found in the framework of DFT approach.
2) a counter-cation-mediated *inter*molecular electron transfer from Pc of one molecule to {V_{12}} of another molecule. As a result of this process, two states are generated: one-electron reduced, and electron deficient which give rise to an unpaired electron at {V_{12}} and at Pc, respectively. The latter state cannot be detected by r.t. EPR if Ln is paramagnetic, but its existence can be inferred from the fact that Pc is the most probable donor in this system. The existence of this process is confirmed by DFT and MD.

AC-magnetometry revealed that Dy-based compounds are field induced single molecule magnets with the mono compound giving the strongest out-of-phase signal. Measurements of a diluted sample for mono compound and theoretical calculations imply that the relaxation process at low temperature is dominated by the quantum tunnelling induced by magnetic dipolar interactions between Dy^{III} ions as well as between a Dy^{III} ion and an unpaired electron delocalized over the {$V_{12}O_{32}$} core or Pc. Magnetochemical modelling of the PcDy-{V_{12}} indicates that there is a weak antiferromagnetic interaction between Dy^{III} and unpaired electron located at Pc or {V_{12}}, which is consistent with DFT results.

The obtained results persuade us to further research this type of responsive nanocomposites with the far-reaching goal of their future implementation into molecularly powered classic and quantum sensor/computing technologies.[97] The challenging goals here are (1) to generate entanglement between two magnetic states (of delocalized electron and Ln) e.g. by means of

electric field[98], (2) to reveal the effect[99] of external magnetic field on the lifetime of charge-separated states, and (3) to incorporate functional PcLn-{V_{12}} and (PcLn)$_2$-{V_{12}} as active switching components into highly ordered two- or three-dimensional porous frameworks.

We are currently performing large-area electron transport measurements of the title nanocomposites on suitable substrate surfaces, which will be reported elsewhere. The latter studies should provide answers to the effect of an external electric field[100] on the magnetic state of an entire molecular nanocomposite resulting between other from moving the delocalized electron in or out of the exchange contact with Ln.

ASSOCIATED CONTENT

The Supporting Information including general methods, synthetic procedure, analytical and crystallographic data, computational study and magnetochemical modelling is available free of charge via the Internet at http://pubs.acs.org. CCDC 2153157, 2144215, 2144214, 2144213, 2153158, 2153159, 2144216.

AUTHOR INFORMATION

Corresponding Author

* Kirill Yu. Monakhov – Leibniz Institute of Surface Engineering (IOM), Permoserstr. 15, 04318 Leipzig, Germany. E-mail: kirill.monakhov@iom-leipzig.de
* Xavier López – Universitat Rovira i Virgili, Departament de Química Física i Inorgànica, Marcel·lí Domingo 1, 43007 Tarragona, Spain. E-mail: javier.lopez@urv.cat
* Piotr Kozłowski – Institute of Spintronics and Quantum Information, Faculty of Physics, Adam Mickiewicz University in Poznań, ul. Uniwersytetu Poznańskiego 2, 61-614 Poznań, Poland. E-mail: kozl@amu.edu.pl

Author Contributions

I.W., X.L., P.K., A.K. and K.Y.M. co-wrote the manuscript. I.W. performed synthesis, spectroscopic data analysis and electrochemical study. J.G. conducted EPR spectroscopy. A.M.-S. and X.L. performed computational study. K.Z. carried out DC and AC SQUID measurements and P.K. performed magnetochemical modelling. A.K. performed photo- and radiation chemical study. M.B. performed X-ray analysis. Z.W. and J.W. performed mass spectrometry. K.Y.M. conceived, initiated, and supervised the study.

Notes

The authors declare no competing financial interest.

[§]The fluorescence quantum yields should be considered as the upper limit, since already marginal residual amounts (< 0.1%) of free base phthalocyanines from the syntheses may contribute substantially to the observed fluorescence.

ACKNOWLEDGMENT

This work was supported by the Individual Research Grant (project number: 432224404) of the Deutsche Forschungsgemeinschaft (DFG). Magnetochemical calculations were carried out at Poznań Supercomputing and Networking Centre in Poznań, Poland. K.Z. acknowledges the financial support from the National Science Centre of Poland by the SONATA Project No. UMO-2016/23/D/ST3/02121. The authors are also grateful to late Prof. Stefan Jurga from NanoBioMedical Centre, Adam Mickiewicz University in Poznań (Poland) for the possibility of conducting magnetic measurements in the Centre. X.L. acknowledges the grant PID2020-112762GB-I00 funded by the MCIN/AEI/10.13039/501100011033. J.W. acknowledges a Freigeist-Fellowship of the Volkswagen Foundation. The authors express their gratitude to Prof. H. Krautscheid (Leipzig University) for the access to the STOE Stadivari diffractometer and A. Prager (IOM, Leipzig) for performing the XPS measurements.

REFERENCES

(1) Pope, M. T.; Kortz, U. Polyoxometalates. In *Encyclopedia of Inorganic and Bioinorganic Chemistry*; John Wiley & Sons, 2012. DOI: 10.1002/9781119951438.eibc0185.pub2
(2) Long, D.-L.; Tsunashima, R; Cronin, L. Polyoxometalates: Building Blocks for Functional Nanoscale Systems. *Angew. Chem., Int. Ed.* **2010**, *49*, 1736–1758.
(3) Misra, A; Kozma, K; Streb, C; Nyman, M. Beyond Charge Balance: Counter-cations in Polyoxometalate Chemistry. *Angew. Chem., Int. Ed.* **2020**, *59*, 596–612.
(4) Gumerova, N. I.; Rompel; A. Polyoxometalates in Solution: Speciation Under Spotlight. *Chem. Soc. Rev.* **2020**, *49*, 7568–7601.
(5) Cameron, J. M.; Guillemot, G.; Galambos, T.; Amin, S. S.; Hampson, E.; Haidaraly, K. Mall; Newton, G. N.; Izzet, G. Supramolecular Assemblies of Organo-functionalized Hybrid Polyoxometalates: from Functional Building Blocks to Hierarchical Nanomaterials. *Chem. Soc. Rev.* **2022**, *51*, 293–328.
(6) Anyushin, A. V.; Kondinski, A.; Parac-Vogt, T. N. Hybrid Polyoxometalates as Post-functionalization Platforms: from Fundamentals to Emerging Applications. *Chem. Soc. Rev.* **2020**, *49*, 382–432.
(7) Izzet, G.; Volatron, F.; Proust, A. Tailor-made Covalent Organic-Inorganic Polyoxometalate Hybrids: Versatile Platforms for the Elaboration of Functional Molecular Architectures. *Chem. Rec.* **2017**, *17*, 250–266.
(8) Sanvito, S. Molecular Spintronics. *Chem. Soc. Rev.* **2011**, *40*, 3336–3355.
(9) Forment-Aliaga, A; Coronado, E. Hybrid Interfaces in Molecular Spintronics. *Chem. Rec.* **2018**, *18*, 737–748.
(10) Stuckart, M.; Monakhov, K. Yu. Polyoxometalates as Components of Supramolecular Assemblies. *Chem. Sci.* **2019**, *10*, 4364–4376.
(11) Gumerova, N. I.; Rompel, A. Synthesis, Structures and Applications of Electron-rich Polyoxometalates. *Nat. Rev. Chem.* **2018**, *2*, 0112.
(12) Dreiser, J. Molecular Lanthanide Single-ion Magnets: from Bulk to Submonolayers. *J. Phys.: Condens. Matter* **2015**, *27*, 183203.
(13) a) Ritchie, C.; Boskovic, C. Polyoxometalates as Ligands for Functional Lanthanoid Complexes. In *Polyoxometalate Chemistry Some Recent Trends*; World Scientific, 2013; pp 177–214; b) Vonci, M.; Boskovic, C. *Aust. J. Chem.* **2014**, *67*, 1542–1552; c) Ritchie, C.; Baslon, V.; Moore, E. G.; Reber, C.; Boskovic, C. Sensitization of Lanthanoid Luminescence by Organic and Inorganic Ligands in Lanthanoid-organic-polyoxometalates. *Inorg. Chem.* **2012**, *51*, 1142–1151.
(14) Costa-Coquelard, C.; Sorgues, S.; Ruhlmann, L. Photocatalysis with Polyoxometalates Associated to Porphyrins under Visible Light: An Application of Charge Transfer in Electrostatic Complexes. *J. Phys. Chem. A* **2010**, *114*, 6394–6400.
(15) Ahmed, I.; Farha, R.; Goldmann, M.; Ruhlmann, L. *Chem. Commun.* **2013**, *49*, 496–498.

(16) Pamin,K.; Prończuk, M.; Basąg, S.; Kubiak, W.; Sojka, Z.; Połtowicz, J. A New Hybrid Porphyrin-heteropolyacid Material: Synthesis, Characterization and Investigation as Catalyst in Baeyer–Villiger Oxidation. Synergistic Effect. *Inorg. Chem. Commun.* **2015**, *59*, 13–16.

(17) Panagiotopoulos, A.; Douvas, A. M.; Argitis, P.; Coutsolelos, A. G. Porphyrin-sensitized Evolution of Hydrogen using Dawson and Keplerate Polyoxometalate Photocatalysts. *ChemSusChem* **2016**, *9*, 3213–3219.

(18) Natali, M.; Deponti, E.; Vilona, D.; Sartorel, A.; Bonchio, M.; Scandola, F. A Bioinspired System for Light-driven Water Oxidation with a Porphyrin Sensitizer and a Tetrametallic Molecular Catalyst. *Eur. J. Inorg. Chem.* **2015**, 3467–3477.

(19) Song, Y. F.; Tsunashima, R. Recent Advances on Polyoxometalate-based Molecular and Composite Materials. *Chem. Soc. Rev.* **2012**, *41*, 7384–7402.

(20) Radivojevic, I.; Ithisuphalap, K.; Burton-Pye, B. P.; Saleh, R.; Francesconi, L. C.; Drain, C. M. Ternary Phthalocyanato Hf(IV) and Zr(IV) Polyoxometalate Complexes. *RSC Adv.* **2013**, *3*, 2174–2177.

(21) Sarwar, S.; Sanz, S.; Van Leusen, J.; Nichol, G. S.; Brechin, E. K.; Kögerler, P. Phthalocyanine-polyoxotungstate Lanthanide Double Deckers. *Dalton Trans.* **2020**, *49*, 16638–16642.

(22) Linnenberg, O.; Moors, M.; Notario-Estévez, A.; López, X.; De Graaf, C.; Peter, S.; Baeumer, C.; Waser, R.; Monakhov, K. Yu. Addressing Multiple Resistive States of Polyoxovanadates: Conductivity as a Function of Individual Molecular Redox States. *J. Am. Chem. Soc.* **2018**, *140*, 16635–16640.

(23) Stuckart, M.; Izarova, N. V.; Glöß, M.; Klose, J.; Schmitz-Antoniak, C.; Koegerler, P.; Kersting, B.; Monakhov, K. Yu. Insertion of V^{IV} Ions into the Polyoxotungstate Archetype $\{As_4W_{40}\}$. *Inorg. Chem.* **2021**, *60*, 8437–8441.

(24) Monakhov, K. Yu.; Bensch, W.; Koegerler, P. Semimetal-functionalised Polyoxovanadates. *Chem. Soc. Rev.* **2015**, *44*, 8443–8483.

(25) Stuckart, M.; Monakhov, K. Yu. Vanadium: Polyoxometalate Chemistry. In *Encyclopedia of Inorganic and Bioinorganic Chemistry*; John Wiley & Sons, 2012. DOI: 10.1002/9781119951438.eibc2615

(26) Putt, R.; Kozłowski, P.; Werner, I.; Griebel, G.; Schmitz, S.; Warneke, J.; Monakhov, K. Yu. $\{P_2V_3W_{15}\}$-Polyoxometalates Functionalized with Phthalocyaninato Y and Yb Moieties. *Inorg. Chem.* **2021**, *60*, 80–86.

(27) Putt, R.; Qiu, X.; Kozłowski, P.; Gildenast, H.; Linnenberg, O.; Zahn, S.; Chiechi, R. C.; Monakhov, K. Yu. Self-assembled Monolayers of Polyoxovanadates with Phthalocyaninato Lanthanide Moieties on Gold Surfaces. *Chem. Commun.* **2019**, *55*, 13554–13557.

(28) Okaya, K.; Kobayashi, T.; Koyama, Y.; Hayashi, Y.; Isobe, K. Formation of V^V Lacunary Polyoxovanadates and Interconversion Reactions of Dodecavanadate Species. *Eur. J. Inorg. Chem.* **2009**, *2009*, 5156–5163.

(29) Kastner, K.; Forster, J.; Ida, H.; Newton, G. N.; Oshio, H.; Streb, C. Controlled Reactivity Tuning of Metal-functionalized Vanadium Oxide Clusters. *Chem. Eur. J.* **2015**, *21*, 7686–7695.

(30) Kastner, K.; Lechner, M.; Weber, S.; Streb, C. *In Situ* Assembly, De-metalation and Induced Repair of a Copper-polyoxovanadate Oxidation Catalyst. *ChemistrySelect* **2017**, *2*, 5542–5544.

(31) Anjass, M.; Kastner, K.; Nagele, F.; Ringenberg, M.; Boas, J. F.; Zhang, J.; Bond, A. M.; Jacob, T.; Streb, C. Stabilization of Low-valent Iron(I) in a High-valent Vanadium(V) Oxide Cluster. *Angew. Chem., Int. Ed.* **2017**, *56*, 14749–14752.

(32) Seliverstov, A.; Streb, C. A New Class of Homogeneous Visible-Light Photocatalysts: Molecular Cerium Vanadium Oxide Clusters. *Chem. Eur. J.* **2014**, *20*, 9733–9738.

(33) Cameron, J. M.; Newton, G. N.; Busche, C.; Long, D. L.; Oshio, H.; Cronin, L. Synthesis and Characterisation of a Lanthanide-capped Dodecavanadate Cage. *Chem. Commun.* **2013**, *49*, 3395–3397.

(34) Šimuneková, M.; Prodius, D.; Mereacre, V.; Schwendt, P.; Turta, C.; Bettinelli, M.; Speghini, A.; Lan, Y.; Anson, C. E.; Powell, A. K. Tetradecanuclear Lanthanide-vanadium "Nanochocolates": Catalytically-active Cationic Heteropolyoxovanadium Clusters. *RSC Adv.* **2013**, *3*, 6299–6304.

(35) Schwarz, B.; Durr, M.; Kastner, K.; Heber, N.; Ivanovic-Burmazovic, I.; Streb, C. Solvent-controlled Polymerization of Molecular Strontium Vanadate Monomers into 1D Strontium Vanadium Oxide Chains. *Inorg. Chem.* **2019**, *58*, 11684–11688.

(36) Greiner, S.; Schwarz, B.; Ringenberg, M.; Durr, M.; Ivanovic-Burmazovic, I.; Fichtner, M.; Anjass, M.; Streb, C. Redox-inactive Ions Control the Redox-activity of Molecular Vanadium Oxides. *Chem. Sci.* **2020**, *11*, 4450–4455.

(37) Greiner, S.; Schwarz, B.; Streb, C.; Anjass, M. Effect of Heterometal-functionalization and Template Exchange on the Redox Chemistry of Molecular Vanadium Oxides. *Chem. Eur. J.* **2021**, *27*, 1–8.

(38) Chen, J. J.; Symes, M. D.; Cronin, L. Highly Reduced and Protonated Aqueous Solutions of $[P_2W_{18}O_{62}]^{6-}$ for On-demand Hydrogen Generation and Energy Storage. *Nat. Chem.* **2018**, *10*, 1042–1047.

(39) Bouvet, M.; Bassoul, P.; Simon, J. Synthesis and Electrical Properties of a New Molecular Semiconductor: The Unsymmetrical Lutetium Phthalo-Naphthalocyanine. *Mol. Cryst. Liq. Cryst.* **1994**, *252*, 31–38.

(40) Trojan, K. L.; Hatfield, W. E.; Kepler, K. D.; Kirk, M. L. Strong Exchange Coupling in Lanthanide Bis-(phthalocyaninato) Sandwich Compounds. *J. Appl. Phys.* **1991**, *69*, 6007–6009.

(41) Winslow, F. H.; Baker, W. O.; Yager, W. A. Odd Electrons in Polymer Molecules. *J. Am. Chem. Soc.* **1955**, *77*, 4751–4756.

(42) Eyer, G. P.; Kittilstved, K. R.; Andrew, T. L. Anomalous Paramagnetism in Closed-shell Molecular Semiconductors. *J. Phys. Chem. C* **2017**, *121*, 24929–24935.

(43) Monakhov, K. Yu.; Linnenberg, O.; Kozłowski, P.; Van Leusen, J.; Besson, C.; Secker, T.; Ellern, A.; López, X.; Poblet, J. M.; Kögerler, P. Supramolecular Recognition Influences Magnetism in $[X@HV^{IV}_8V^V_{14}O_{54}]^{6-}$ Self-Assemblies with Symmetry-Breaking Guest Anions. *Chem. Eur. J.* **2015**, *21*, 2387–2397.

(44) Müller, A.; Pope, M. T.; Todea, A. M.; Bogge, H.; Van Slageren, J.; Dressel, M.; Gouzerh, P.; Thouvenot, R.; Tsukerblat, B; Bell, A. Metal-oxide-based Nucleation Process under Confined Conditions: Two Mixed-valence V_6-Type Aggregates Closing the W_{48} Wheel-type Cluster Cavities. *Angew. Chem., Int. Ed.* **2007**, *46*, 4477–4480.

(45) Linnenberg, O.; Kozłowski, P.; Besson, C.; Van Leusen, J.; Englert, U.; Monakhov, K. Yu. A V_{16}-type Polyoxovanadate Structure with Intricate Electronic Distribution: Insights from Magnetochemistry. *Cryst. Growth Des.* **2017**, *17*, 2342–2350.

(46) Augustyniak-Jablokow, M. A.; Borshch, S. A.; Daniel, C.; Hartl, H.; Yablokov, Y. V. EPR Study of the Magnetic States of a Mixed-valence $V^{IV}_4V^V_2$ Alkoxypolyoxovanadium Cluster. *New J. Chem.* **2005**, *29*, 1064–1071.

(47) Lapham, P.; Vila-Nadal, L.; Cronin, L.; Georgiev, V. P. Influence of the Contact Geometry and Counterions on the Current Flow and Charge Transfer in Polyoxometalate Molecular Junctions: A

Density Functional Theory Study. *J. Phys. Chem. C* **2021**, *125*, 3599–3610.

(48) Tsunashima, R.; Nakamura, I.; Oue, R.; Koga, S.; Oki, H.; Noro, S. I.; Nakamura, T.; Akutagawa, T. Inter-cluster Distance Dependence of Electrical Properties in Single Crystals of a Mixed-valence Polyoxometalate. *Dalton. Trans.* **2017**, *46*, 12619–12624.

(49) Rinehart, J. D.; Long, J. R. Exploiting Single-ion Anisotropy in the Design of f-Element Single-molecule Magnets. *Chem. Sci.* **2011**, *2*, 2078–2085.

(50) a) Komijani, D.; Ghirri, A.; Bonizzoni, C.; Klyatskaya, S.; Moreno-Pineda, E.; Ruben, M.; Soncini, A.; Affronte, M.; Hill, S. Radical-lanthanide Ferromagnetic Interaction in a Tb^{III} Bis-phthalocyaninato Complex. *Phys. Rev. Mater*. **2018**, *2*, 024405; b) Ishida, T.; Nakamura, T.; Kihara, T.; Nojiri, H. Chemical Trend on the Lanthanide-radical Exchange Coupling. *Polyhedron* **2017**, *136*, 149–154; c) Urdampilleta, M.; Klayatskaya, S.; Ruben, M.; Wernsdorfer, W. Magnetic Interaction Between a Radical Spin and a Single-molecule Magnet in a Molecular Spin-valve. *ACS Nano* **2015**, *9*, 4458–4464; d) Huang, H.; Van den Heuvel, W.; Soncini, A. Lanthanide-radical Magnetic Coupling in $[LnPc_2]^0$: Competing Exchange Mechanisms Captured via Ab Initio Multi-Reference Calculations. *Quantum Mater*. *Res*. **2020**, *1*, e200003, and references therein.

(51) Rast, S.; Borel, A.; Helm, L.; Belorizky, E.; Fries, P. H.; Merbach, A. E. EPR Spectroscopy of MRI-related Gd(III) Complexes: Simultaneous Analysis of Multiple Frequency and Temperature Spectra, Including Static and Transient Crystal Field Effects. *J. Am. Chem. Soc.* **2001**, *123*, 2637–2644.

(52) Zhang, X.; Xie, H.; Ballesteros-Rivas, M.; Woods, T. J.; Dunbar, K. R. Conducting Molecular Nanomagnet of Dy^{III} with Partially Charged TCNQ Radicals. *Chem. Eur. J.* **2017**, *23*, 7448–7452.

(53) Oliver, W. D.; Welander, P. B. Materials in Superconducting Quantum Bits. *MRS Bulletin* **2013**, *38*, 816–825.

(54) Van der Spoel, D.; Lindahl, E.; Hess, B.; Groenhof, G.; Mark, A. E.; Berendsen, H. J. GROMACS: Fast, Flexible, and Free. *J. Comput. Chem.* **2005**, *26*, 1701–1718.

(55) Hess, B.; Kutzner, C.; Van der Spoel, D.; Lindahl, E. GROMACS 4: Algorithms for Highly Efficient, Load-balanced, and Scalable Molecular Simulation. *J. Chem. Theory Comput.* **2008**, *4*, 435–447.

(56) Wang, J.; Cieplak, P.; Kollman, P. A. How Well Does a Restrained Electrostatic Potential (RESP) Model Perform in Calculating Conformational Energies of Organic and Biological Molecules? *J. Comput. Chem.* **2000**, *21*, 1049–1074.

(57) Chaumont, A.; Wipff, G. Polyoxometalate Keggin Anions at Aqueous Interfaces with Organic Solvents, Ionic Liquids, and Graphite: A Molecular Dynamics Study. *J. Phys. Chem. C* **2009**, *113*, 18233–18243.

(58) Jiménez-Lozano, P.; Solé-Daura, A.; Wipff, G.; Poblet, J. M.; Chaumont, A.; Carbó, J. J. Assembly Mechanism of Zr-containing and Other TM-containing Polyoxometalates. *Inorg. Chem.* **2017**, *56*, 4148–4156.

(59) Toupalas, G.; Karlsson, J.; Black, F. A.; Masip-Sánchez, A.; López, X.; Ben M'Barek, Y.; Blanchard, S.; Proust, A.; Alves, S.; Chabera, P.; Clark, I. P.; Pullerits, T.; Poblet, J. M.; Gibson, E. A.; Izzet, G. Tuning Photoinduced Electron Transfer in POM-Bodipy Hybrids by Controlling the Environment: Experiment and Theory. *Angew. Chem., Int. Ed.* **2021**, *60*, 6518–6525.

(60) Te Velde, G.; Bickelhaupt, F. M.; Baerends, E. J.; Fonseca Guerra, C.; Van Gisbergen S. J. A.; Snijders, J. G.; Ziegler, T. Chemistry with ADF. *J. Comput. Chem.* **2001**, *22*, 931–967.

(61) ADF 2019.3, SCM, Theoretical Chemistry, Vrije Universiteit, Amsterdam, The Netherlands, http://www.scm.com.

(62) Swart, M.; Ehlers, A. W.; Lammertsma, K. Performance of the OPBE Exchange-correlation Functional. *Mol. Phys.* **2004**, *102*, 2467–2474.

(63) Becke, A. D. Density-functional Thermochemistry. III. The Role of Exact Exchange. *J. Chem. Phys.* **1993**, *98*, 5648–5652.

(64) Stephens, P. J.; Devlin, F. J.; Chabalowski, C. F.; Frisch, M. J. Ab Initio Calculation of Vibrational Absorption and Circular Dichroism Spectra Using Density Functional Force Fields. *J. Phys. Chem. A* **1994**, *98*, 11623–11627.

(65) Van Lenthe, E.; Baerends, E. J.; Snijders, J. G. Relativistic Regular Two-component Hamiltonians. *J. Chem. Phys.* **1993**, *99*, 4597–4610.

(66) Van Lenthe, E.; Baerends, E. J.; Snijders, J. G. Relativistic Total Energy Using Regular Approximations. *J. Chem. Phys.* **1994**, *101*, 9783–9792.

(67) Van Lenthe, E.; Ehlers, A.; Baerends, E. J. Geometry Optimizations in the Zero Order Regular Approximation for Relativistic Effects. *J. Chem. Phys.* **1999**, *110*, 8943–8953.

(68) Pye, C. C.; and Ziegler, T. An Implementation of the Conductor-like Screening Model of Solvation Within the Amsterdam Density Functional Package. *Theor. Chem. Acc.* **1999**, *101*, 396–408.

(69) Buxton, G. V. Radiation Chemistry of the Liquid State. In *Radiation Chemistry – Principles and Applications*; VCH Publ. Inc., 1987; pp 321–350.

(70) Wardman, P. Reduction Potentials of One-Electron Couples Involving Free Radicals in Aqueous Solution. *J. Phys. Chem. Ref. Data* **1989**, *18*, 1637–1723.

(71) Ishii, K; Kobayashi, N. The Photophysical Properties of Phthalocyanines and Related Compounds. In *The Porphyrin Handbook*, Vol. 16; Academic Press, 2000; pp. 1–42.

(72) Kahnt, A. Photophysical Characterization of Porphyrinoids. In *Applications of Porphyrinoids as Functional Materials*; The Royal Society of Chemistry, 2021; pp 220–251.

(73) Guldi, D. M.; Zilbermann, M. I.; Gouloumis, A.; Vázquez, P.; Torres, T. Nanoscale Organization of a Phthalocyanine−fullerene System: Remarkable Stabilization of Charges in Photoactive 1-D Nanotubules. *J. Phys. Chem. B* **2004**, *108*, 18485–18494.

(74) FitzGerald, S.; Farren, C.; Stanley, C. F; Beeby, A.; Bryce, M. R. Fluorescent Phthalocyanine Dimers – a Steady State and Flash Photolysis Study. *Photochem. Photobiol. Sci.* **2002**, *1*, 581–587.

(75) Farren, C.; FitzGerald, S.; Beeby, A.; Bryce, M. R. The First Genuine Observation of Fluorescent Mononuclear Phthalocyanine Aggregates. *Chem. Commun.* **2002**, 572–573.

(76) Imahori, H.; Hagiwara, K.; Aoki, M.; Akiyama, T.; Taniguchi, S.; Okada, T.; Shirakawa, M.; Sakata, Y. Linkage and Solvent Dependence of Photoinduced Electron Transfer in Zincporphyrin-C_{60} Dyads. *J. Am. Chem. Soc.* **1996**, *118*, 11771–11782.

(77) Wolf, M.; Villegas, C.; Trukhina, O.; Delgado, J. L.; Torres, T.; Martín, N.; Clark, T.; Guldi, D. M. Mediating Reductive Charge Shift Reactions in Electron Transport Chains. *J. Am. Chem. Soc.* **2017**, *139*, 17474–17483.

(78) Nikolaou, V.; Plass, F.; Planchat, A.; Charisiadis, A.; Charalambidis, G.; Angaridis, P. A.; Kahnt, A.; Odobel, F.; Coutsolelos, A. G. Effect of the Triazole Ring in Zinc Porphyrin-fullerene Dyads on the Charge Transfer Processes in NiO-based Devices. *Phys. Chem. Chem. Phys.* **2018**, *20*, 24477–24489.

(79) Pyatosi, V. E.; Tsvirko, M. P. Triplet-triplet Absorption Spectra of Phthalocyanine and Its Metal Complexes. *J. Appl. Spectrosc.* **1980**, *33*, 869–872.

(80) El-Khouly, M. E.; Ito, O.; Smith, P. M.; D'Souza, F. Intermolecular and Supramolecular Photoinduced Electron Transfer Processes of Fullerene–porphyrin/phthalocyanine Systems. *J. Photochem. Photobiol. C: Photochem. Rev.* **2004**, *5*, 79–104.

(81) Nyokong, T.; Gasyna, Z.; Stillman, M. J. Phthalocyanine *p*-Cation-radical Species: Photochemical and Electrochemical Preparation of $[ZnPc(-1))^{+}$ in Solution. *Inorg. Chem.* **1987**, *26*, 548–553.

(82) Ough, E.; Gasyna, Z.; Stillman, M. J. Photochemical, Electrochemical, and Chemical Formation of the *p*-Cation-radical Species of Magnesium Phthalocyanine. Analysis of the Absorption and MCD Spectra of $[MgPc(-1)]^{+}$. *Inorg. Chem.* **1991**, *30*, 2301–2310.

(83) Minor, P. C.; Gouterman, M.; Lever, A. B. P. Electronic Spectra of Phthalocyanine Radical Anions and Cations. *Inorg. Chem.* **1985**, *24*, 1894–1900.

(84) Seitz, W.; Kahnt, A.; Guldi, D. M.; Torres, T. Controlling Charge Transfer in Fullerene/Phthalocyanine Electron Donor-acceptor Conjugates/Hybrids. *J. Porphyr. Phthalocyanines* **2009**, *13*, 1034–1039.

(85) Moreno-Pineda, E.; Wernsdorfer, W. Measuring Molecular Magnets for Quantum Technologies. *Nat. Rev. Phys.* **2021**, *3*, 645–659.

(86) Atzori, M.; Sessoli, R. The Second Quantum Revolution: Role and Challenges of Molecular Chemistry. *J. Am. Chem. Soc.* **2019**, *141*, 11339–11352.

(87) Wasielewski, M. R.; Forbes, M. D. E.; Frank, N. L.; Kowalski, K.; Scholes, G. D.; Yuen-Zhou, Y.; Baldo, M. A.; Freedman, D. E.; Goldsmith, R. H.; Goodson, T.; Kirk, M. L.; McCusker, J. K.; Ogilvie, J. P.; Shultz, D. A.; Stoll, S.; Whaley, K.B. Exploiting Chemistry and Molecular Systems for Quantum Information Science. *Nat. Rev. Chem.* **2020**, *4*, 490–504.

(88) Coronado, E. Molecular Magnetism: From Chemical Design to Spin Control in Molecules, Materials and Devices. *Nat. Rev. Mat.* **2020**, *5*, 87–104.

(89) Ishikawa, R.; Michiwaki, S.; Noda, T.; Katoh, K.; Yamashita, M.; Kawata, S. Series of Chloranilate-bridged Dinuclear Lanthanide Complexes: Kramers Systems Showing Field-induced Slow Magnetic Relaxation. *Magnetochemistry* **2019**, *5*, 30.

(90) Wada, H.; Ooka, S.; Iwasawa, D.; Hasegawa, M.; Kajiwara, T. Slow Magnetic Relaxation of Lanthanide(III) Complexes with a Helical Ligand. *Magnetochemistry* **2016**, *2*, 43.

(91) Topping, C. V.; Blundell, S. J. A.C. Susceptibility as a Probe of Low-frequency Magnetic Dynamics. *J. Phys. Condens. Matter* **2019**, *31*, 013001.

(92) Ding, Y. S.; Yu, K. X.; Reta, D.; Ortu, F.; Winpenny, R. E. P.; Zheng, Y. Z.; Chilton, N. F. Field- and Temperature-dependent Quantum Tunnelling of the Magnetisation in a Large Barrier Single-molecule Magnet. *Nat. Commun.* **2018**, *9*, 3134.

(93) Bartolome, E.; Arauzo, A.; Luzon, J.; Bartolome, J.; Bartolome, F. Magnetic Relaxation of Lanthanide-Based Molecular Magnets. In *Handbook of Magnetic Materials*, Vol. 26; North Holland, 2017; pp 1–289.

(94) Aravena, D. Ab Initio Prediction of Tunneling Relaxation Times and Effective Demagnetization Barriers in Kramers Lanthanide Single-Molecule Magnets. *J. Phys. Chem. Lett.* **2018**, *9*, 5327–5333.

(95) Ardavan, A.; Rival, O.; Morton, J. J.; Blundell, S. J.; Tyryshkin, A. M.; Timco, G. A.; Winpenny, R. E. Will Spin-relaxation Times in Molecular Magnets Permit Quantum Information Processing? *Phys. Rev. Lett.* **2007**, *98*, 057201.

(96) Sorensen, M. A.; Hansen, U. B.; Perfetti, M.; Pedersen, K. S.; Bartolome, E.; Simeoni, G. G.; Mutka, H.; Rols, S.; Jeong, M.; Zivkovic, I.; Retuerto, M.; Arauzo, A.; Bartolome, J.; Piligkos, S.; Weihe, H.; Doerrer, L. H.: Van Slageren, J.; Ronnow, H. M.; Lefmann, K.; Bendix, J. Chemical Tunnel-splitting-engineering in a Dysprosium-based Molecular Nanomagnet. *Nat. Commun.* **2018**, *9*, 1292.

(97) Gaita-Ariño, A.; Luis, F.; Hill, S.; Coronado, E. Molecular Spins for Quantum Computation. *Nat. Chem*. **2019**, *11*, 301–309.

(98) Palii, A.; Aldoshin, S.; Tsukerblat, B.; Borràs-Almenar, J. J.; Clemente-Juan, J. M.; Cardona-Serra, S.; Coronado, E. Electric Field Generation and Control of Bipartite Quantum Entanglement between Electronic Spins in Mixed Valence Polyoxovanadate $[GeV_{14}O_{40}]^{8-}$. *Inorg. Chem*. **2017**, *56*, 9547–9554.

(99) Miura, T.; Fujiwara, D.; Akiyama, K.; Horikoshi,, T.; Suzuki, S.; Kozaki, M.; Okada, K.; Ikoma, T. Magnetic Control of the Charge-separated State Lifetime Realized by Covalent Attachment of a Platinum Complex. *J. Phys. Chem. Lett.* **2017**, *8*, 661–665.

(100) Cardona-Serra, S.; Clemente-Juan, J. M.; Coronado, E.; Gaita-Ariño, A.; Suaud, N.; Svoboda, O.; Bastardis, R.; Guihéry, N.; Palacios, J. J. Electrically Switchable Magnetic Molecules: Inducing a Magnetic Coupling by Means of an External Electric Field in a Mixed-Valence Polyoxovanadate Cluster. *Chem. Eur. J*. **2015**, *21*, 763–769.

TOC graphic